Front-end Electronics for Silicon Photomultipliers

von

Johannes Schumacher

Masterarbeit in Physik

vorgelegt der
Fakultät für Mathematik, Informatik und Naturwissenschaften
der
Rheinisch-Westfälischen Technischen Hochschule Aachen

im Januar 2014

angefertigt am

III. Physikalischen Institut A

betreut durch

Univ.-Prof. Dr. Thomas Hebbeker

Gutachter und Betreuer   Zweitgutachter

Prof. Dr. Thomas Hebbeker   Dr. Oliver Pooth
III. Physikalisches Institut A   III. Physikalisches Institut B
RWTH Aachen   RWTH Aachen

Contents

Abstract

In der nahen Zukunft versprechen Silizium Photomultiplier (SiPMs) die nächste Generation der Standarddetektoren in der Hochenergiephysik zu werden. Auch in der Astroteilchenphysik haben SiPMs bereits Fuß gefasst. FAMOUS ist ein Fluoreszenz Teleskop Prototyp zur Detektion ultrahochenergetischer kosmischer Luftschauer und basiert auf SiPMs anstatt auf traditionellen Photomultiplier Tubes (Kapitel 1). SiPMs zeigen u.a. Temperaturabhängigkeiten und müssen dementsprechend auf ihre Eigenschaften untersucht werden. Zu diesen Eigenschaften zählen das Rauschen und der Gain (Kapitel 2). Weitere Parametere von SiPMs, wie die Photodetektionseffizienz (PDE) und das zeitliche Verhalten, müssen ebenso charakterisiert werden.

Im Rahmen seiner Masterarbeit hat der Autor Front-end Elektronik entwickelt, mit dessen Hilfe SiPMs ausgelesen und charakterisiert werden können. Zunächst wird ein elektronisches Ersatzschaltbild eines SiPMs vorgestellt (Kapitel 2). Passive und aktive Strom-Spannungs-Wandler werden miteinander verglichen. Vom Autor wird die aktive Variante bevorzugt und in den weiteren Kapiteln übernommen.

Das nächste Kapitel befasst sich mit wichtigen elektronischen Eigenschaften realer Operationsverstärker (op-amps), insbesondere mit dem limitierten frequenzabhängigen Ansprechen und dem elektronischen Rauschen (Kapitel 3). Die Front-end Elektronik wird vorgestellt.

Labormessungen mit der Front-end Elektronik werden im letzten Teil durchgeführt (Kapitel 4). Dieses Kapitel fängt mit der Vermessung einer Reihe von Operationsverstärkern an. Dabei wird insbesondere auf das Ansprechen und elektronische Rauschen eingegangen. Außerdem wird gezeigt, dass mit der hier vorgestellten Front-end Elektronik die Temperaturabhängigkeit des Gains des SiPMs herauskorrigiert werden kann.

Der Autor schließt seine Masterarbeit mit einer kurzen Zusammenfassung der wichtigsten Eigenschaften seiner Front-end Elektronik ab und gibt einen Ausblick auf die weitere Arbeit der FAMOUS Gruppe an der RWTH Aachen.

Silicon photomultipliers (SiPMs) promise to be the next generation photo detectors in high-energy physics. SiPMs have taken root also in astroparticle physics. FAMOUS is a fluorescence telescope prototype for the detection of ultra-high energy cosmic air showers and makes use of SiPMs instead of traditional photomultiplier tubes (chapter 1). SiPMs need to be characterised with regard to their intrinsic parameters, like temperature dependence, noise and gain (chapter 2).

In his master thesis, the author has developed front-end electronics for the characterisation of SiPMs. At first, the equivalent circuit of an SiPM model is introduced (chapter 2). Ideal read-out circuits in terms of passive and active current-to-voltage conversion are compared. It is shown why the active version is preferred.

The next part deals with important features of real operational amplifiers (op-amps), especially with limited frequency response and electronic noise (chapter 3). The front-end electronics is introduced.

Measurements with the front-end electronics are done in the last part (chapter 4). It starts with the characterisation of a selection of op-amps, especially frequency response and electronic noise. Also, measurements of the SiPM gain stability with the temperature compensation unit are demonstrated.

The author concludes his master thesis with a short summary of the properties of his front-end electronics and gives a brief outlook into the future work of the FAMOUS group at RWTH Aachen University.

1. Introduction

1.1 Cosmic rays and extensive air showers

For over a century, physicists around the world have tried to uncover the mystery of cosmic ray induced extended air showers. In 1912, Austrian-American physicist Victor Franz Hess has proven that the radiation has cosmic origin by measuring the ionisation in air [1]. Over the years, scientists developed stationary and mobile experiments to measure cosmic ray particles. Directly - with airborne experiments like balloons, satellites and recently with telescopes and underground neutrino detectors or indirectly at the surface of the Earth by recording the profile of the air shower when the cosmic ray particle collides with molecules in the atmosphere of the Earth. Down to the present day, the sources of ultra high-energy cosmic rays are still unknown.

The energy spectrum spreads over 30 decades of flux to energies up to $100 \, \mathrm{EeV} = 10^{20} \, \mathrm{eV}$ and the flux per energy bin is usually given in units of one over Area $\times$ Time $\times$ Energy [3]. It is marvellous that the energy spectrum is well described by simple power laws $N(E) \propto E^{-\gamma}$ while the spectral index γ depends on the energy range and varies between 2.7 and 3.1 [4]. The variation of γ with energy leads to conspicuous features in the energy spectrum, see figure 1.1. These features can be interpreted as a transition of galactic to extra-galactic sources. But this has not been confirmed yet.

The study of ultra high-energy cosmic rays is of special interest: Due to their high momentum, the gyroradii of the particles become very high. Therefore, ultra high-energy particles travel through space without being deflected notably by magnetic fields. Hence, the arrival direction on the surface of the Earth will point approximately to the source of the cosmic ray.

Between $10^{19} \, \mathrm{eV}$ and $10^{20} \, \mathrm{eV}$, the cosmic ray flux is suppressed dramatically. The most common explanation is the Greisen-Zatsepin-Kuzmin limit (also known as GZK cut-off) introduced individually by K. Greisen [5] and G. T. Zatsepin and V. A. Kuz'min [6] in 1966: Ultra high-energy protons interact with cosmic microwave background (CMB) photons γ_{CMB} and produce a short-lived Δ^+ resonance which immediately decays into a neutral pion π^0 or charged pion π^+ and a proton p or neutron n, respectively [2]
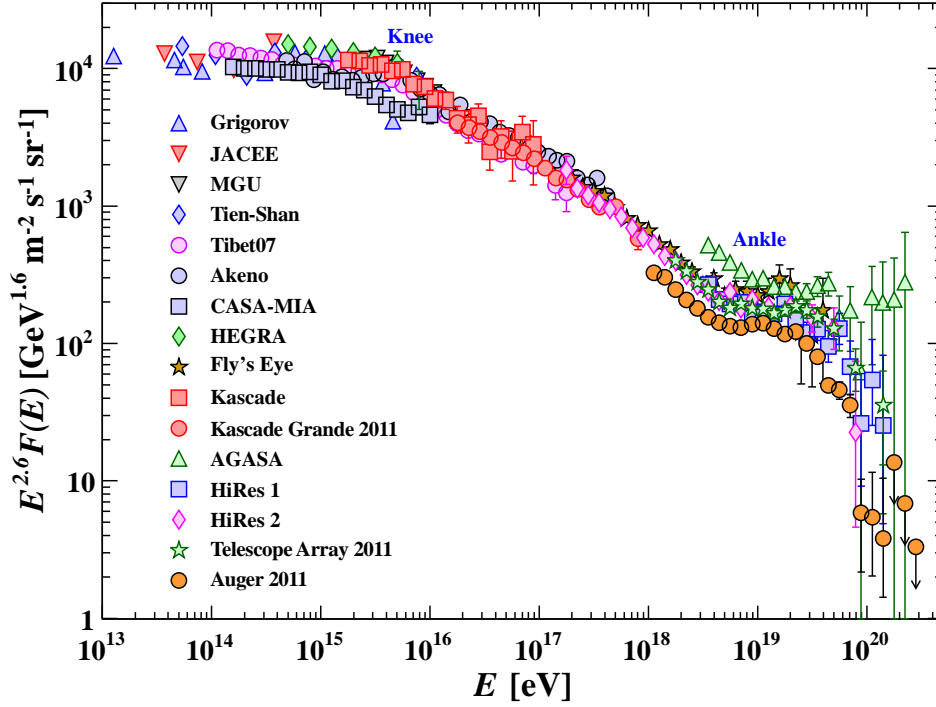
Figure 1.1: The cosmic ray spectrum at the highest energies, scaled by $E^{2.6}$ which gives a more impressive view on the cosmic ray features, like the *knee* and *ankle*. The plot combines the results of several experiments until 2012. Strong discrepancies are visible. This graphic is taken from [2].

$$p + \gamma_{\mathrm{CMB}} \rightarrow \Delta^+ \rightarrow p + \pi^0$$
$$\text{or} \rightarrow n + \pi^+.$$

The high energy incident particle will lose roughly 20% of its energy. The cut-off energy is between $10^{19}\,\mathrm{eV}$ and $10^{20}\,\mathrm{eV}$ [6]. Another (even simpler) explanation is that the energy reachable in the cosmic accelerator is finite. The question of the origin of cosmic rays is still unanswered. Possible source candidates are supernovae and AGNs, among others. Identifying the cosmic accelerator is one of several open questions that may be hopefully answered by astroparticle physics experiments in the next years.

Electromagnetic cascades can be accurately described by applying the Heitler model. The energy of the primary particle E_{primary} can be obtained analytically from

$$X_{\max} \propto \ln\left(E_{\mathrm{primary}}\right), \tag{1.1}$$

see [4], if the air shower only contains an electromagnetic component. A parameterisation of the lateral particle density introduced in [7] applies also to Hadronic shower components and is frequently used to parameterise data obtained by experiments

$$N(X) = N_{\max} \left(\frac{X - X_1}{X_{\max} - X_1} \right)^{\frac{X_{\max} - X_1}{\lambda}} \exp \left(\frac{X_{\max} - X}{\lambda} \right), \qquad (1.2)$$

where $N_{\max} \equiv N(X_{\max})$ is the number of particles at shower depth $X_{\max}$, X_1 is the energy-dependent atmospheric depth of the first interaction of the primary particle and λ is the interaction length of the primary particle, depending on its energy and mass and likewise given in $\mathrm{g\,cm^{-2}}$. Equation (1.2), also known as Gaisser-Hillas-formula, can be fitted to measured data of air showers from which one is able to extract X_1 and λ easily, see next section. By comparing the measured $N(X)$ with air shower simulations, one is able to obtain properties of the primary particle, like chemical composition, energy and direction.

1.2 The Pierre Auger Observatory

From fig. 1.1, one can see that the flux of ultra high-energy cosmic rays above $1\,\mathrm{EeV}$ is very low. To achieve higher statistics, the only adjustable parameters are time and area. The Pierre Auger Observatory is currently the largest experiment specialised in cosmic ray physics [9]. The experiment covers $3000\,\mathrm{km^2}$ of the Argentine Pampas[1] and uses a hybrid detection technique: 1660 on-ground surface detectors (SD), see fig. 1.3 based on the water Cherenkov detector principle, measure secondary particles of the cosmic air shower. These secondary particles are relativistic, the velocity is higher than the speed of light in water. According to the Cherenkov principle, Cherenkov light will be generated when these particles pass the SD tank. The light is measured by three photomultiplier tubes.

The coincidence measurement in multiple SD stations allows to recreate the lateral footprint of the shower on the ground. The shower footprint can be parameterised to obtain a robust energy estimator. One of the big advantages of SD is the high duty cycle of nearly 100% [10].

27 fluorescence telescopes at four detector sites (FD) measure fluorescence light, generated mostly by de-exciting Nitrogen in the atmosphere after reacting with secondary particles [8]. Schematics of one FD telescope can be found in figure 1.4. The longitudinal profile of the shower measured by FD can be used to do calorimetric measurements and to obtain the energy of the primary particle. $X_{\max}$ is an important parameter, which describes the atmospheric depth of the maximal expansion of the air shower.

The FD optics is based on a Schmidt camera design. The optical sensors of FD are XP3062 photomultiplier tubes (PMTs). The quantum efficiency (QE) of these

---

[1]For comparison: The total area of Saarland (federal state of Germany) is less than $2600\,\mathrm{km^2}$.
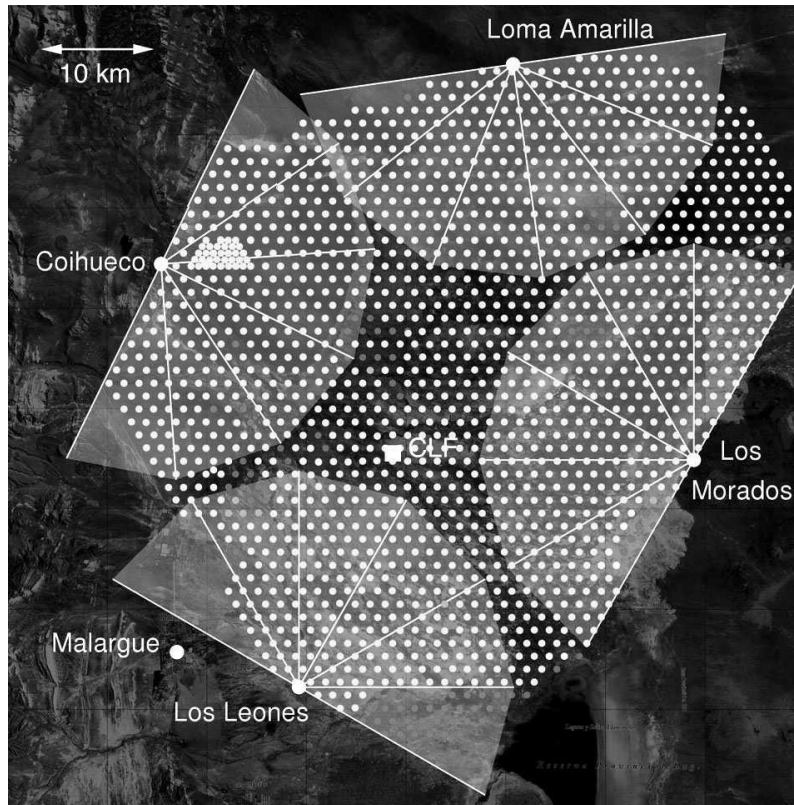
Figure 1.2: The Pierre Auger Observatory delineated in a map of the Argentine Pampas as of March 2009, taken from [8]. Light dots represent Surface Detector (SD) stations. The shaded semicircles indicate the field of views of the Fluorescence Detector (FD) stations, each one of them houses six fluorescence telescopes.

PMTs is about 25% averaged over wavelengths from 350 nm to 400 nm [8]. 440 PMTs are arranged in each camera where hexagonal cones concentrate the light on the photocathode of the PMTs. UV transmitting filters reduce the background noise of the night sky since fluorescence light is mostly bluish and UV-like, see figure 1.5.

Several upgrades have already been performed, planned and considered in the last few years. "The High Elevation Auger Telescope" (HEAT) represents a low energy[2] extension of the Pierre Auger Observatory [13]. HEAT consists of three FD telescopes, each tilted by roughly 29° to monitor air showers with lower X_{max} and therefore smaller primary energies E_{primary}. The optics of HEAT are very similar to standard FD. HEAT is deployed near the Auger Engineering Array (also known as "infill" array) in the northwest corner of the array, near the Coihueco FD site.

The "Auger Engineering Radio Array" (AERA) measures the radio component created by secondary particles between 30 MHz and 80 MHz which is locally free of man-made radio frequencies. 160 AERA antenna stations have been deployed and are operating since September 2010 on a 20 km^2 grid and 150 m spacing in the infill array. Like SD, the duty cycle reaches 100%. The angular resolution is very high

---

[2]approximately one order of magnitude below the 24 standard FD telescopes, thus down to 10^{17} eV [12].

Figure 1.3: A photograph of a typical surface detector (SD) station taken by the author. This detector type is based on the water Cherenkov principle. Particles passing the tank faster than the speed of light in water will generate Cherenkov light cones. This is measured by 3 photomultiplier tubes.
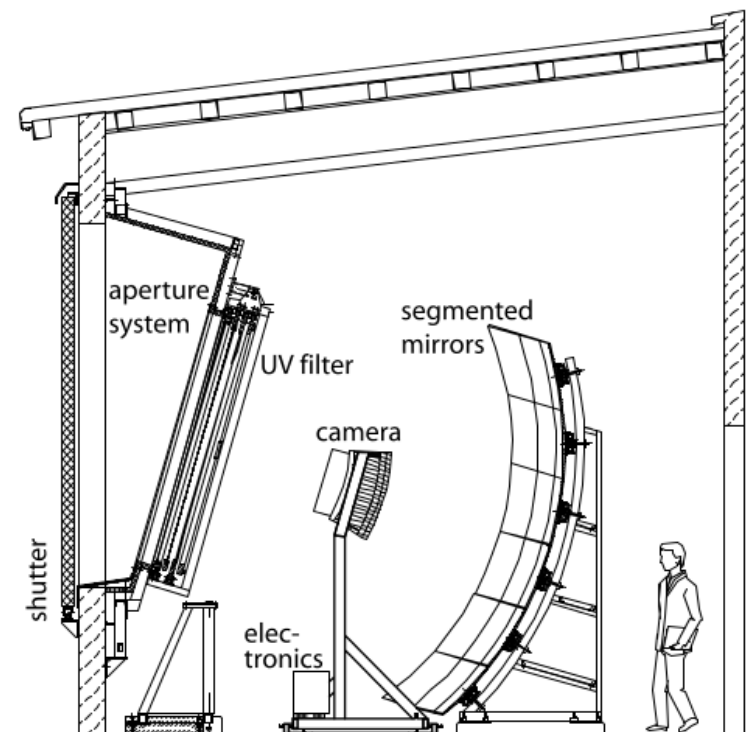
Figure 1.4: Schematics of one fluorescence detector (FD) telescope. These telescopes are based on Schmidt camera optics, see text. The detectors are kept in a cool and dry environment inside the building. The shutters on the front are opened in moonless nights only. The image is taken from [8].
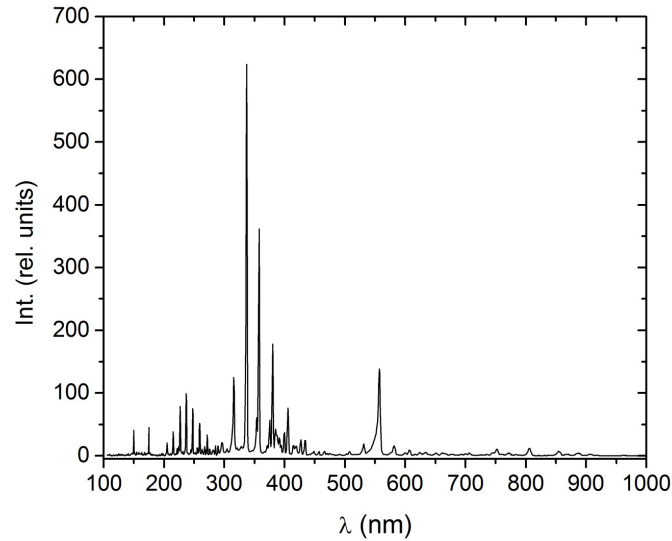
Figure 1.5: The spectrum, intensity vs. wavelength, of fluorescence light. The intensity between 300 nm and 400 nm is mostly created by de-exciting Nitrogen in the atmosphere after being excited by secondary particles in the extended air shower. Plot taken from [11].

which allows gathering geometric information of the shower. The gain of the radio signal is proportional to the energy squared [14].

The "Auger Muons and Infill for the Ground Array" (AMIGA) upgrade consists of 61 water Cherenkov detectors (WCD) like the SD stations on a $25\,km^2$ grid with a spacing of 750 m. This increases the sensitivity of the detector by one decade in energy. Underground scintillators buried near AMIGA-WCDs are specialised Muon counters which separate the electromagnetic from the Muon component of the air shower, giving a good energy estimator as well as discriminating between primary compositions [15].

1.3   FAMOUS

In 2010, development started to design a fluorescence telescope prototype named FAMOUS (First Auger MPPC camera for the Observation of Ultra high-energy cosmic air Showers) at III. Physikalisches Institut A, RWTH Aachen University, Germany, which makes use of silicon photomultipliers (SiPMs) for optical read-out [16]. Since SiPMs are quite small, only a few mm^2 in size, see chapter 2, the layout of FAMOUS is based on a refractive design using a Fresnel lense, see figure 1.6. At the beginning of 2013, the seven pixel version FAMOUS[7] measured first light in Aachen which has mainly been night-sky background. FAMOUS is being upgraded to the full 64 pixel version.

Figure 1.6: This photo (taken early in 2013) shows the FAMOUS[7] fluorescence detector prototype from behind. Four cables are attached to the front-end electronics of FAMOUS[7]. The Fresnel lens cannot be seen on this photo. The photo has been taken by Tim Niggemann.

2. Silicon Photomultipliers

This chapter deals with a new photon detection technique: *silicon photomultipliers* (SiPMs). These semiconductors are based on *avalanche photodiode* (APD) arrays. While *photomultiplier tubes* (PMTs), which are traditionally used for light detection in high energy physics, are limited in *quantum efficiency* (QE), SiPMs promise a higher photon detection efficiency (PDE) and are not influenced by magnetic fields.

In the introductory chapter, the main characteristics of SiPMs are presented. Advantages and disadvantages are described and discussed. Basic understanding of Laplace circuit transform is indispensable. The last part deals with electronic properties of SiPMs and describes electronic read-out techniques based on an equivalent SiPM circuit. Analytical calculations are being introduced which are used in the following chapters.

Notice that all voltages are denoted with respect to ground potential ($V_{\mathrm{GND}} \equiv 0\,\mathrm{V}$) unless otherwise specified.

2.1 Introduction

The development of silicon photomultipliers (SiPMs) has started in 1993 [17]. First SiPMs have consisted of 10^4 *avalanche photodiode* (APD) cells based on titanium and silicon carbide layers covering an area of $1\,\mathrm{mm}^2$ [18]. The *cell pitch*, which is the edge length of one square cell, has been $10\,\mu\mathrm{m}$. Today's SiPMs usually have cell pitches between $25\,\mu\mathrm{m}$ and $100\,\mu\mathrm{m}$ to reach higher relative sensitive areas, also known as *fill factor*. The fill factor is defined by the ratio of the active area to the total area of the SiPM. A larger fill factor grants a higher *photon detection efficiency* (PDE) [19]. The cells are operating in Geiger-mode which means that the APD is counting photons only and no information about the energy of the photon or number of simultaneously arriving photons per cell is preserved. A photo of a modern SiPM (Hamamatsu S10362-33-050C) is shown in figure 2.1.

The *breakdown voltage* v_{bd} is an intrinsic parameter of SiPMs. After applying a *bias voltage* $v_b > v_{\mathrm{bd}}$ accross the SiPM, an electric field is generated which accelerates free charge carriers. The voltage excess of the bias voltage v_b applied to the SiPM with respect to the breakdown voltage v_{bd} is known as the *overvoltage*

$$v_{\mathrm{ov}} \equiv v_b - v_{\mathrm{bd}}. \tag{2.1}$$
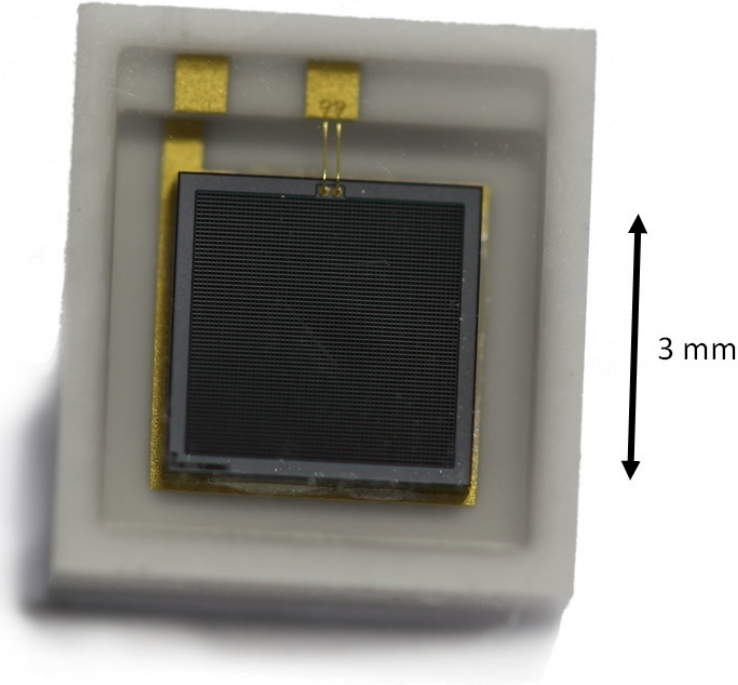
Figure 2.1: Photo of an Hamamatsu S10362-33-050C silicon photomultiplier (SiPM) taken by the author. This $3 \times 3\,\mathrm{mm}^2$ module has 3600 cells, $50 \times 50\,\mu\mathrm{m}^2$ each, and has been used for several measurements in this thesis. Anode and cathode are clearly visible (golden contacts on the top). In figure A.12, a microscope image of the very same SiPM is shown.

It is known that the breakdown voltage increases linearly with temperature T

$$v_{\mathrm{bd}}(T) = v_{\mathrm{bd}}(T_0) + \beta\,(T - T_0)\,, \tag{2.2}$$

see [20] [21], where $T_0 \equiv 0\,^{\circ}\mathrm{C}$. $\beta = \mathrm{const.}$ depends on the SiPM type and varies between $10\,\mathrm{mV}\,^{\circ}\mathrm{C}^{-1}$ and $100\,\mathrm{mV}\,^{\circ}\mathrm{C}^{-1}$. For example, β of Hamamatsu SiPMs based on series S10362 is roughly $56\,\mathrm{mV}\,^{\circ}\mathrm{C}^{-1}$ [22], whereas β of Excelitas SiPMs based on the C30742 series is typically $90\,\mathrm{mV}\,^{\circ}\mathrm{C}^{-1}$ [23]. This means that the overvoltage as defined in equation (2.1) is decreasing linearly with temperature for constant v_b. Many properties of the SiPM like gain, (correlated) noise effects and PDE depend on the overvoltage. These properties have to be characterised at constant temperature or at least at constant overvoltage.

The dominating noise effect on longer time-scales is thermal noise, generated randomly by thermally induced charge carriers [20]. Electrons and holes of an avalanche may recombine in an APD cell generating a photon which can be detected in another cell. This is called *optical crosstalk*. This noise effect can be reduced by adding trenches between individual cells and is currently introduced in the manufacturing process of SiPMs [24] [25]. The third noise effect is entitled *afterpulsing*. This effect
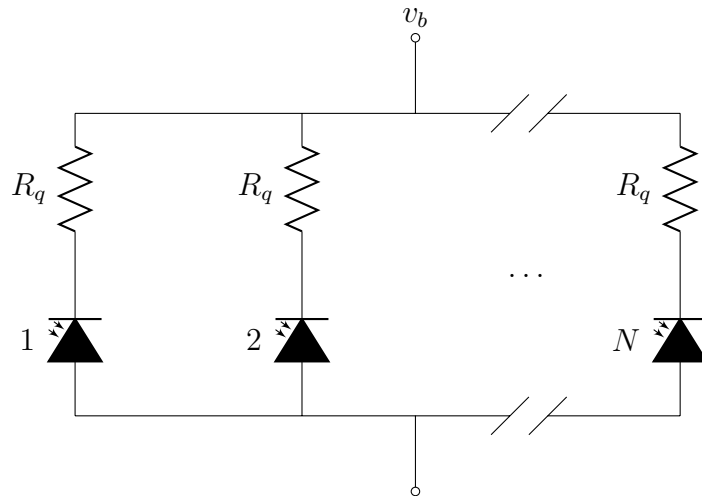
Figure 2.2: A single silicon photomultiplier (SiPM) consisting of N G-APD cells (including series quenching resistor R_q) which are connected in parallel. The cells share the same bias voltage v_b which is applied at the cathode (the top in this drawing). Each photodiode symbol represents one G-APD here.

dominates especially in impurified silicon and can be reduced by producing purer silicon. Free carriers are blocked within the silicon due to lattice scattering and can create an avalanche in the same cell shortly after [21].

SiPMs have become popular over the years due to their great potential for experiments - especially in elementary particle physics. The high gain and the insensitivity to magnetic fields allows the deployment of SiPMs in medical physics, e.g. Positron emission tomography (PET). Today's prototypes of SiPMs achieve PDEs of 50% [26] and even up to and beyond 60% [27] in the near UV range, typically above 400 nm. The PDE of commercially available SiPMs, on the other hand, is approx. 35% in the near UV, depending on the overvoltage [21].

The moderate operating voltage of $v_b < 100$ V, reasonable prices below 100 € [24], compactness (few mm^2) and robustness [22] [23] [26] are advantages, especially for small, portable experiments. The main disadvantage of this light detector is the temperature dependence, see equation (2.2) and correlated noise. These effects have been studied extensively at III. Physikalisches Institut A/B, RWTH Aachen University, for example in [20] [21] and are well understood by now. Also, the small size of these devices can be disadvantageous when a large active area is needed.

Electronically speaking, the APD cells of the SiPM are connected in parallel, sharing the same bias voltage v_b applied to the whole SiPM, see figure 2.2. Each cell has a series quenching resistor R_q. If the voltage drop across the APD becomes larger than the intrinsic breakdown voltage v_{bd} of the diode, the energy will be high enough to accelerate electron-hole pairs across the junction, created by a triggered photon or noise. A current is generated leading to a voltage drop at the quenching resistor R_q. The voltage accross the diode decreases, the electric field vanishes and no charge carriers are accelerated through the junction anymore. Thus the avalanche process

is "quenched". Because no current flows through the diode at this time, the voltage at the diode increases again, reaching v_{bd}. From now on, the APD is sensitive to photons again. If no avalanche is triggered, the voltage across the APD will reach v_b once more.

2.2   Laplace transform

Calculations of electronic circuits can be simplified by transforming from time domain (t-domain) into the complex frequency domain (s-domain) [28]. Since t-domain solutions must be calculated from first order linear differential equations like

$$i(t) = C \frac{d}{dt} v(t),$$

a transform is chosen such that equations of this type turn into a linear algebraic equation

$$I(s) = sCV(s) - Cv(t \to 0^-).$$

Here, $v(t \to 0^-)$ is the voltage at the capacitor C before $t = 0$. The current I is constrained by the voltage that has been applied before $t = 0$. The transformation is done by using the Laplace transform

$$F(s) = \int_{0^-}^{\infty} dt\, f(t)\, e^{-s\,t},$$

see appendix A. The Laplace transform is a linear operator. The transformed equations can be solved much easier than systems of linear differential equations. After being solved, these equations can be retransformed into the t-domain by applying the inverse transformation, see appendix.

In this thesis, the Laplace transform will be applied to many electronic circuits. Most of these transformations will be solved using computer algebra software, e.g. MAPLE. Small symbols for currents $i(t)$ and voltages $v(t)$ represent t-domain quantities while capital letters $I(s)$ and $V(s)$ stand for s-domain equivalents. Notice that t-domain constant voltages and currents are not constant in the s-domain and vice versa $v = \text{const.} \Rightarrow V(s) = v/s$.
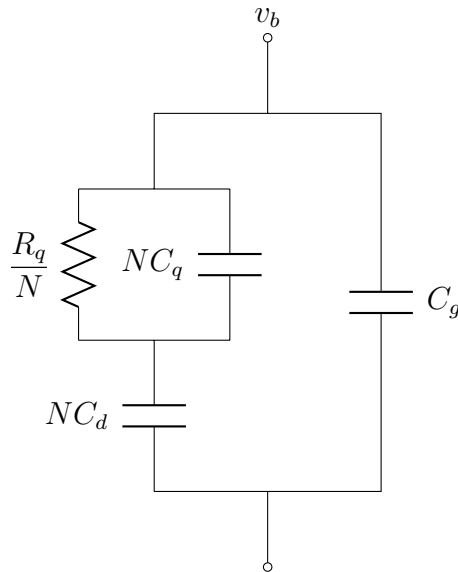
Figure 2.3: Electronic model of a single silicon photomultiplier (SiPM) consisting of N cells. Time-domain (t-domain) equivalent circuit, based on the design proposed in [29], see also fig. 2.4.

2.3   Electronic circuits

This section introduces the SiPM model that is used to calculate and simulate front-end circuits in this thesis. At first, the SiPM equivalent model is introduced. Secondly, mathematical methods are used for calculating the signal output of the SiPM analytically, based on the equivalent circuit of the SiPM. At the end, two types of read-out circuits are compared: The passive current-to-voltage conversion using a shunt resistor R_s plus an inverting operational amplifier (op-amp), and the active current-to-voltage conversion using a transimpedance amplifier. The active conversion will be used in the next chapters.

2.3.1   SiPM equivalent circuit

One of the first electronic models of SiPMs has been developed by F. Corsi et al in 2006 [29] [30]. It consists of N electronically parallel cells; each cell has a quenching resistor R_q and a parasitic capacitance C_q, in series with a simplified equivalent circuit of a photodiode represented solely by the capacitance of the diode C_d, see fig. 2.3. Typical values for these parameters are $R_q = \mathcal{O}(100\,\mathrm{k}\Omega)$, $C_q, C_d = \mathcal{O}(100\,\mathrm{fF})$. The impedance of one cell is thus

$$Z_{\mathrm{cell}}(s) = \left(R_q \parallel \frac{1}{sC_q} \right) + \frac{1}{sC_d}.$$

C_g "summarises" additional parallel parasitic effects, like the metal routing grid, see photo in fig. 2.1. Since all cells are connected in parallel, they can be combined by using standard impedance rules, because

$$Z_{\text{SiPM}}(s) = Z_{\text{cell}}(s) \ || \ Z_{\text{cell}}(s) \ || \ \cdots + \frac{1}{sC_g}$$

$$= \frac{Z_{\text{cell}}(s)}{N} + \frac{1}{sC_g}$$

$$= \left(\frac{R_q}{N} \ || \ \frac{1}{sNC_q} \right) + \frac{1}{sNC_d} + \frac{1}{sC_g},$$

see fig. 2.3. Let us now assume that $M < N$ cells are triggered simultaneously, which leaves $N - M$ cells untriggered. The avalanche process can be described by a very short current pulse $i_d(t)$ of $\mathcal{O}(\text{ps})$ in parallel to the diode capacitance

$$i_d(t) = M \, Q \, \delta(t)$$
$$\Leftrightarrow I_d(s) = M \, Q$$

where Q is the charge released during an avalanche by one cell. $I_d(s)$ is the Laplace transform of $i_d(t)$, see table A.1 in the appendix, with

$$Q = v_{\text{ov}}(C_q + C_d), \tag{2.3}$$

see figure 2.4 [29]. An extensive derivation has been motivated by the author of this master thesis and printed in the appendix, see A. At this point it must be said that equation 2.3 is only an approximation. For small breakdown timespans and vanishingly small diode resistances during breakdown, equation 2.3 becomes true. To understand this derivation, the reader shall finish this chapter first, since the motivation in the appendix is based on figures and results of the next few subsections.

2.3.2 SiPM read-out circuits

SiPMs are current sources. Usually, experimentalists deal with voltages instead of currents, for example by using analogue-to-digital converters. The main task of this subsection is the conversion of the SiPM output current to a proportional voltage.

2.3.2.1 Passive current-to-voltage conversion

A basic read-out can be arranged by adding a shunt resistor R_s to ground, see fig. 2.5. R_s is a low ohmic resistor (typically $50 \, \Omega$) which converts the current into a proportional voltage. To increase the gain, an inverting op-amp is commonly proposed [22]. The differential voltage $V_D = V_+ - V_-$ at the input nodes of an ideal op-amp is

$$V_D = 0$$
$$\Leftrightarrow V_+ - V_- = 0.$$
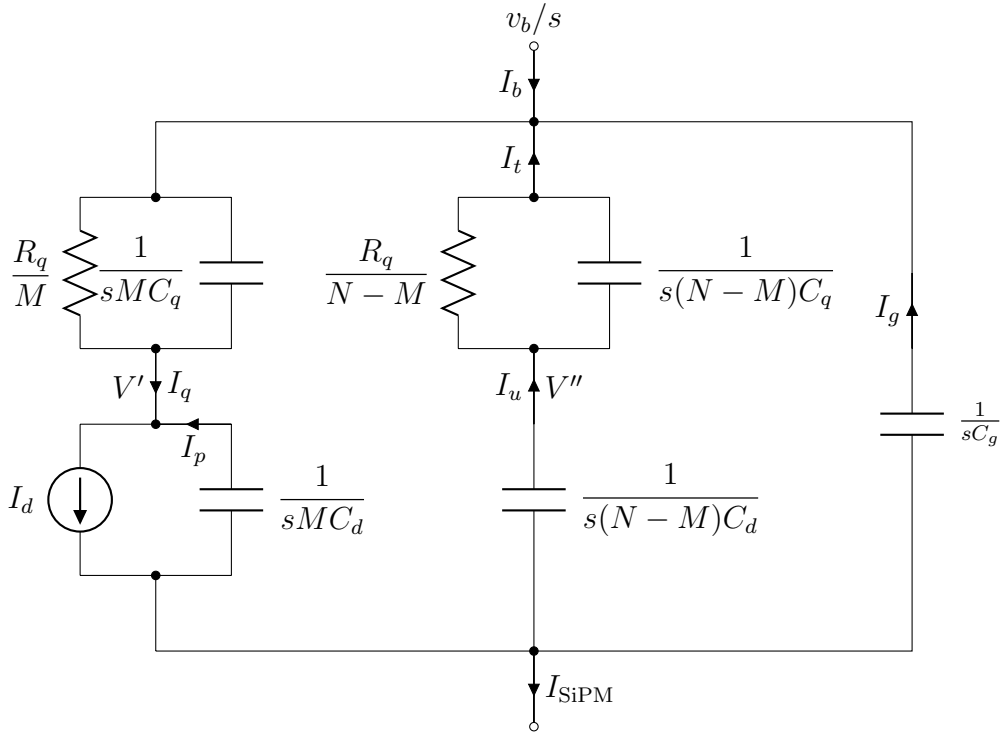
Figure 2.4: Electronic model of a single silicon photomultiplier (SiPM) consisting of N cells of which $M < N$ cells have been triggered by an avalanche. s-domain equivalent circuit, based on the design proposed in [29]. Instead of drawing this model every time, a photodiode symbol will be used from now on. The direction of the currents are marked in the circuit and are used in the calculations.

$V_\pm$ is the voltage at the non-inverting and inverting input of the op-amp, respectively. Above equation holds only for ideal op-amps. For real op-amps, $V_D \neq 0$ because of the limited open loop gain. Since V_+ is connected to ground, the voltage at the inverting input V_- also becomes 0 (known as *virtual ground*). An ideal op-amp draws no current at the input nodes because of its infinitely high input impedance.

By applying Kirchhoff's circuit and voltage laws, as well as Laplace integral transforms, see chapter A, the t-domain voltage drop at the output of the amplifier $v_o(t)$ can be calculated analytically. The following calculations have been done by the author using MAPLE. First of all, the circuit is transformed into the s-domain equivalent using Laplace transforms, see again chapter A for basic transformation rules.

A t-domain constant voltage $v_b(t) = \text{const.} \Rightarrow V_b(s) = v_b/s$ is applied at the SiPM cathode which is the top part of the SiPM model in figure 2.4. For $t \to 0^-$, no current is drawn in the shunt resistor R_s which means that the t-domain equivalent of the voltage node V''' (as defined in figure 2.5) is at ground potential at that time, i.e. $v'''(t \to 0^-) = 0\,\text{V}$. This invokes a voltage drop at the capacitors MC_d, $(N-M)C_d$ and C_g which is equal to $MC_d v_b$, $(N-M)C_d v_b$ and $C_g v_b$, respectively. However, no voltage drops at MC_q and $(N-M)C_q$ since $v'(t \to 0^{-1}) = v_b$ because
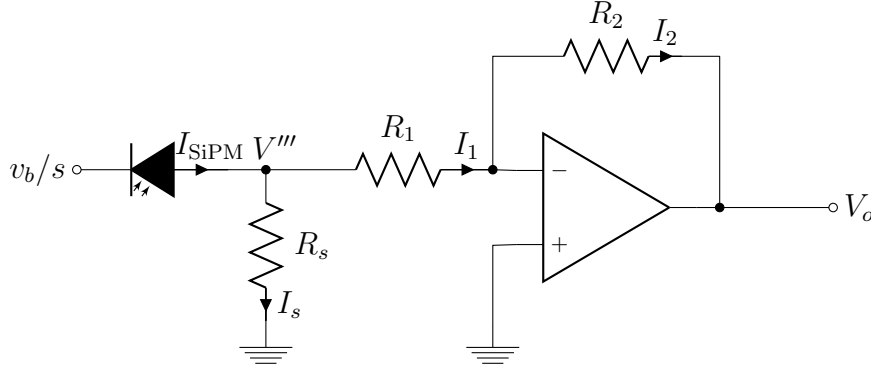
Figure 2.5: An SiPM (represented by the photodiode symbol on the left) read out by a shunt resistor R_s to ground and amplified with an inverting operational amplifier (op-amp). The output voltage $v_o(t)$ in the time domain of an ideal op-amp applied to an SiPM model is defined by eq. (2.8). This circuit is drawn in the s-domain, see text.

no current flows through the quenching resistor R_q/M before the breakdown. The same applies to $v''(t \to 0^-) = v_b$. From fig. 2.4 and fig. 2.5, we can construct the following system of equations

$$
\begin{aligned}
I_d - I_p - I_u - I_g = I_{\text{SiPM}} = I_s + I_1 \\
I_p + I_q = I_d \\
I_u = I_t \\
I_g + I_t + I_b = I_q \\
I_1 = I_2.
\end{aligned}
\tag{2.4}
$$

I_b is the current drawn by the SiPM which flows through its cathode. From those both figures, the following currents can be obtained by using standard impedance and Kirchhoff's rules

$$
\begin{aligned}
I_t &= \frac{V'' - v_b/s}{R_q/(N-M) \,||\, 1/(s(N-M)C_q)} & I_d &= MQ \\
I_q &= \frac{v_b/s - V'}{R_q/M \,||\, 1/(sMC_q)} & I_1 &= \frac{V'''}{R_1} \\
I_g &= \frac{V''' - v_b/s}{1/(sC_g)} + C_g v_b & I_s &= \frac{V'''}{R_s} \\
I_p &= \frac{V''' - V'}{1/(sMC_d)} + MC_d v_b & I_2 &= -\frac{Vo}{R_2} \\
I_u &= \frac{V''' - V''}{1/(s(N-M)C_d)} + (N-M)C_d v_b.
\end{aligned}
\tag{2.5}
$$

This system can be solved for the five unknown parameters I_b, V', V'', V''' and the voltage at the amplifier output V_o by plugging the currents from eq. (2.5) into eq. (2.4) which yields

$$
\begin{aligned}
I_b(s) &= I_b(0) \cdot \frac{1 + a_0 s}{a_1 + a_2 s + a_3 s^2} \\
V'(s) &= V'(0) \cdot \frac{1 + b_0 s + b_1 s^2 + b_2 s^3}{1 + b_3 s + b_4 s^2 + b_5 s^3} \\
V''(s) &= V''(0) \cdot \frac{1 + c_0 s + c_1 s^2 + c_2 s^3}{1 + c_3 s + c_4 s^2 + c_5 s^3} \\
V'''(s) &= V'''(0) \cdot \frac{1 + a_0 s}{a_1 + a_2 s + a_3 s^2} \\
V_o(s) &= -V_o(0) \cdot \frac{1 + a_0 s}{a_1 + a_2 s + a_3 s^2},
\end{aligned}
\tag{2.6}
$$

with

$$
\begin{aligned}
I_b(0) &= MQ\left(1 + R_s/R_1\right) \\
V_o(0) &= MQR_s R_2/R_1 \\
V'''(0) &= MQR_s \\
a_0 &= R_q C_q \\
a_1 &= 1 + R_s/R_1 \\
a_2 &= R_s\left(NC_d + C_g\right) + R_q\left(C_q + C_d\right)\left(1 + R_s/R_1\right) \\
a_3 &= R_q\left(C_q + C_d\right)R_s C_g + N R_q C_q R_s C_d,
\end{aligned}
\tag{2.7}
$$

and Q defined in eq. (2.3). The parameters are chosen such that the summands in the numerator and denominator become unitless. At this point, no solutions for the parameters b_i and c_i are presented, since they are not needed here and the author does not dwell on the t-domain results for V' and V''. From (2.6) we already see that the voltage $v''(t) \neq$ const. v'' is the voltage at the remaining, non-firing diodes of the SiPM. This means, the gain of the remaining cells decreases. The reason for that is the non-zero voltage at the shunt resistor - a disadvantage which has not yet been discussed sufficiently in the literature. We come back to this in section 2.3.2.3.

We apply the inverse Laplace transform to equations (2.6), see table A.1, and finally obtain the voltage drop at the output of the inverting amplifier in the time domain

$$
v_o(t) = -v_o(0)\left(c\, e^{-t/\tau_+} + (1 - c)\, e^{-t/\tau_-}\right),
\tag{2.8}
$$

where (2.3), (2.7) and the following abbrevations hold

$$v_o(0) = V_o(0)\frac{a_0}{a_3}$$
$$c = \frac{1}{2} + \frac{a_2/2 - a_3/a_0}{\sqrt{a_2^2 - 4a_1a_3}}$$
$$\tau_\pm = \frac{2a_3}{a_2 \pm \sqrt{a_2^2 - 4a_1a_3}}. \tag{2.9}$$

The pulse shape at the output of an op-amp operating in the inverting mode and amplifying the signal of a passive current-to-voltage converted SiPM (based on the Corsi model) is thus just the sum of two exponential functions with two different coefficients. This behaviour has been observed in the laboratory and shown in several presentations by many physicists, but never explicitly calculated in detail. The maximum is given by $-v_o(0)$. Obviously, $\tau_+ < \tau_-$. The short exponential function τ_+ is usually called the "spike component". For non-ideal op-amps, this component is becoming so small that it is barely seen. Ultra-high bandwidth op-amps will be needed.

Similar calculations apply to the current that is drawn at the input of the SiPM $i_b(t)$. Using the s-domain results from eq. (2.6) and transforming gives

$$i_b(t) = i_b(0)\left(c\,e^{-t/\tau_+} + (1-c)\,e^{-t/\tau_-}\right), \tag{2.10}$$

with

$$i_b(0) = I_b(0)\frac{a_0}{a_3} \tag{2.11}$$

and the same abbrevations from eq. (2.7) and eq. (2.9). Evaluating $v_o(0)$ and $i_b(0)$ results in

$$v_o(0) = Mv_{\mathrm{ov}}\frac{R_2}{R_1}\frac{1}{C_g/C_q + NC_d/(C_q + C_d)} \tag{2.12}$$
$$i_b(0) = M\frac{v_{\mathrm{ov}}}{R_s}\left(1 + \frac{R_s}{R_1}\right)\frac{1}{C_g/C_q + NC_d/(C_q + C_d)} \tag{2.13}$$
$$\tag{2.14}$$

from which we can deduce that the maximum amplifier output voltage $v_o(0)$ and the maximal current drawn by the SiPM $i_b(0)$ is directly linear to the number of firing cells M and the overvoltage $v_{\mathrm{ov}} = v_b - v_{\mathrm{bd}}$. This is not surprising. In fact, this can easily be reproduced in the laboratory by increasing the light flux and
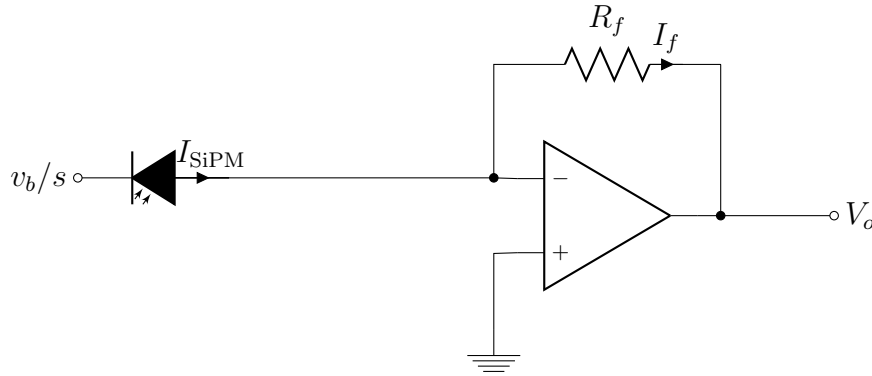
Figure 2.6: An SiPM (represented by the photodiode symbol on the left) read out by a transimpedance amplifier. The output voltage V_o of an ideal op-amp applied to an SiPM model, see chapter 2, is defined by eq. (2.22).

the bias voltage v_b, respectively. Interesting to note, however, is the fact that the maximal voltage is completely independent of the shunt resistor value R_s itself. The parameters of several types of SiPMs have been measured extensively in [31], see table A.3. The voltage drop $v_o(t)$ strongly depends on these values and the maximal voltage drop $v_o(0)$ for a $3 \times 3\,\mathrm{mm}^2$ Hamamatsu SiPM with 3600 cells is well below $R_2/R_1 \times 1\,\mathrm{mV}$. The gain can be varied by changing R_2 and / or R_1.

For $R_s = 50\,\Omega$, $R_1 = 170\,\Omega$ and $R_2 = 680\,\Omega$, the time constants of the two exponential functions become roughly $\tau_+ \approx 5\,\mathrm{ns}$ and $\tau_- \approx 34\,\mathrm{ns}$. The factor is $c \approx 0.8$ which means that the spike component τ_+ dominates the total signal. Apparently, high-speed op-amps $\sim$ GHz are needed to amplify the spike component τ_+ properly. The pulse maximum is about $-2.2\,\mathrm{mV}$.

For a typical $1 \times 1\,\mathrm{mm}^2$ Hamamatsu SiPM with 100 cells, see table A.3, the variables become $\tau_+ < 1\,\mathrm{ns}$, $\tau_- \approx 47\,\mathrm{ns}$ and $c > 0.9$. Here, the SiPM signal is completely dominated by the spike component. Also, the maximal voltage drop is roughly $22.7\,\mathrm{mV}$ which means that the signal is much higher than the signal of the $3 \times 3\,\mathrm{mm}^2$ Hamamatsu SiPM from above. The signal response of a $1 \times 1\,\mathrm{mm}^2$ Hamamatsu SiPM can be seen on the oscilloscope screenshots in the figures A.9 and A.10.

2.3.2.2 Active current-to-voltage conversion

All op-amps in this thesis which are supposed to amplify the SiPM signal are arranged as transimpedance amplifiers. The term "transimpedance" literally describes the mode of operation; a transimpedance amplifier is an active current-to-voltage converter. It consists of an op-amp with a resistor R_f in the negative feedback path. The non-inverting input is connected to ground, see fig. 2.6.

Applying similar calculations like those for a passive *I-V* conversion from the last section to an ideal transimpedance amplifier gives the following:

$$I_p = \frac{0 - V'}{1/(sMC_d)} + MC_d v_b \tag{2.15}$$

$$I_u = \frac{0 - V''}{1/(s(N-M)C_d)} + (N-M)C_d v_b \tag{2.16}$$

$$I_g = \frac{0 - v_b/s}{1/(sC_g)} + C_g v_b \tag{2.17}$$

$$I_f = \frac{0 - V_o}{R_f} \tag{2.18}$$

and the currents I_d, I_q, I_t, and I_b from above, which have to obey the following system of equations

$$
\begin{aligned}
I_d - I_p - I_u - I_g = I_{\text{SiPM}} &= I_f \\
I_p + I_q &= I_d \\
I_u &= I_t \\
I_g + I_t + I_b &= I_q.
\end{aligned}
\tag{2.19}
$$

Solving for I_b, V', V'' and V_o yields

$$
\begin{aligned}
I_b(s) &= I_b(0)\frac{1 + a_0 s}{1 + a_1 s} \\
V'(s) &= v_b \frac{1 + b_0 s}{s + b_1 s^2} \\
V''(s) &= \frac{v_b}{s} \\
V_o(s) &= -V_o(0)\frac{1 + a_0 s}{1 + a_1 s}.
\end{aligned}
\tag{2.20}
$$

with

$$
\begin{aligned}
I_b(0) &= MQ \\
V_o(0) &= MQR_f \\
a_0 &= R_q C_q \\
a_1 &= R_q \left(C_q + C_d\right) \\
b_0 &= R_q \left(C_q + C_d\right) - R_q Q/v_b \\
b_1 &= R_q \left(C_q + C_d\right).
\end{aligned}
\tag{2.21}
$$

Here, $v''(t) = $ const. compared to the passive current-to-voltage conversion which means that the gain is constant for the remaining cells. This will be discussed in section 2.3.2.3. Transforming into the time domain results in the voltage drop at the output of an ideal transimpedance amplifier $v_o(t)$ when fed with a firing SiPM and the current $i_b(t)$ drawn by the SiPM

$$v_{\mathrm{o}}(t) = -MR_f v_{\mathrm{ov}} \frac{C_d}{R_q\left(C_q + C_d\right)} e^{-\frac{t}{R_q(C_q+C_d)}} - MR_f v_{\mathrm{ov}} C_q \delta(t) \qquad (2.22)$$

$$i_{\mathrm{b}}(t) = M v_{\mathrm{ov}} \frac{C_d}{R_q\left(C_q + C_d\right)} e^{-\frac{t}{R_q(C_q+C_d)}} + M v_{\mathrm{ov}} C_q \delta(t). \qquad (2.23)$$

Above symbols are the same like from before. For this configuration, the output is just one exponential function and much easier to derive analytically. The maximal voltage of the SiPM signal and the maximal current drawn by the SiPM, when ignoring the delta distribution, are given as

$$v_o(0^+) = M R_f v_{\mathrm{ov}} \frac{C_d}{R_q\left(C_q + C_d\right)} \qquad (2.24)$$

$$i_b(0^+) = M v_{\mathrm{ov}} \frac{C_d}{R_q\left(C_q + C_d\right)}. \qquad (2.25)$$

Similar to the results from last section, these values depend linearly on the number of firing cells M and the overvoltage v_{ov}. The gain of the output can be increased simply by increasing R_f. The parameters can be evaluated for the two SiPMs, listed in the appendix. For the $3 \times 3\,\mathrm{mm}^2$ SiPM, the transimpedance amplifier with $R_f = 680\,\Omega$ delivers roughly $2.1\,\mathrm{mV}$. The time constant $\tau = R_q(C_q + C_d)$ is smaller than the one of the passive version, about $28\,\mathrm{ns}$. Switching to the $1 \times 1\,\mathrm{mm}^2$ SiPM shows that the time constant τ and the slow time constant of the passive conversion τ_- are very similar, $\tau \approx 46\,\mathrm{ns}$. The pulse height, however, is much lower than the response of the passive version. Ignoring the δ peak results in only $5.7\,\mathrm{mV}$. This is most probably caused by the ignored δ peak. Since this peak can not be amplified by real op-amps, see next chapter, it is fair to ignore this part. If the scientist needs more gain, a two-stage amplifier setting shall be chosen. This will be discussed in detail later.

2.3.2.3 Comparison

The active conversion circuit needs two resistors less than the passive conversion circuit from above. This means, two electronic noise sources less. The total charge drawn by an SiPM read-out by a transimpedance amplifier is given as

$$Q^{\mathrm{active}} = \int_{0^-}^{\infty} dt\, i_b^{\mathrm{active}}(t)$$

$$= M v_{\mathrm{ov}} \left(C_q + C_d\right) \qquad (2.26)$$

which is the current pulse used in the SiPM model, see equation (2.3). Charges are conserved which is a hint that the calculations are correct. Q^{active} is roughly $180\,\mathrm{fC}$

for a single pulse, i.e. $M = 1$, $v_{\mathrm{ov}} = 1\,\mathrm{V}$ and using the parameters from table A.3 for a typical $3 \times 3\,\mathrm{mm}^2$ Hamamatsu SiPM with $50\,\mu\mathrm{m}$ cell pitch.

The voltage in the node between the quenching resistors R_q and the diode capacitance C_d of the non-firing cells $v''(t)$ is not constant for the passive current-to-voltage conversion. This means, if any of these cells fires before $v''(t)$ fully recovers, the gain will be smaller than normal. This will result in an asymmetry when many cells fire within a short time interval. This does not happen with the active conversion. Here, the gain will be stable since $v''(t) = \mathrm{const}$.

Figure 2.7 compares the output voltages of the passive, eq. (2.8), and active, eq. (2.22), current-to-voltage conversion schematically. The gain of the active version is the same like in the front-end boards developed in this thesis. The gain of the passive version is chosen such that the maximum of both versions are equal (the delta distribution in the active version is ignored again) and the feedback resistors R_f and R_2 have the same resistance $R_f = R_2 = 680\,\Omega$. The signal output is plotted for one triggered cell $M \equiv 1$ and two triggered cells $M \equiv 2$.

Apparently, the signal response of the two versions (orange = passive and blue = active in fig. 2.7) look different. The active version is slower than the passive version. This is, because we ignored the delta peak of the active version. Also, the pulse form strongly depends on the shunt resistor R_s and the leading resistor R_1 values. This is a disadvantage of the active version if timing is essential.

2.4   Conclusion

Silicon photomultipliers (SiPMs) are well understood by now. Extensive studies have been performed, for example in the laboratories of RWTH Aachen University. Ray-tracing simulation frameworks for SiPMs have been programmed and electronic models have been developed. In this thesis, a simple model by F. Corsi et al [29] has been chosen to understand the basic performance of SiPMs.

Passive and active current-to-voltage conversions have been calculated analytically. The passive version is proposed by many manufacturers. In this thesis, however, the active version is used.
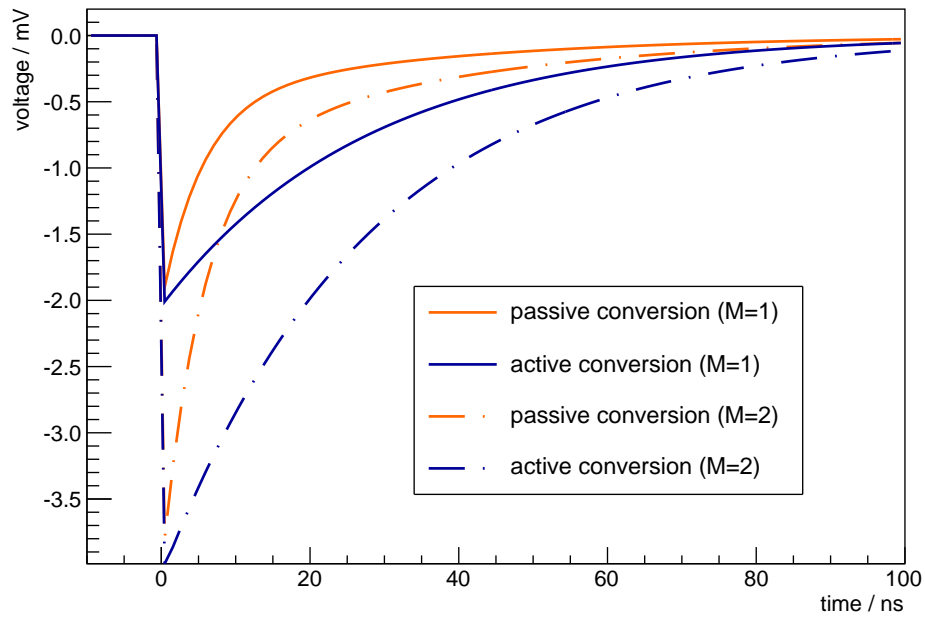
Figure 2.7: This figure shows the passive, eq. (2.8), and active, eq. (2.22) conversion of an SiPM current pulse. In this sketch, the SiPM is modelled by an equivalent circuit and read out by a shunt resistor and inverting op-amp (passive) with $R_s = 50\,\Omega$, $R_1 = 194\,\Omega$, $R_2 = 680\,\Omega$ and an ideal transimpedance amplifier (active) with $R_f = 680\,\Omega$, respectively. Hamamatsu SiPM S10362-33-050C parameters taken from table A.3.

3. Conceptual design of the front-end electronics

The purpose of this thesis is the development of front-end electronics for SiPMs. In this context, front-end electronics is defined as electronics directly located at the SiPM. This includes filtering of the bias voltage v_b, power limitation of the SiPM, (active) current-to-voltage conversion of the SiPM signal via transimpedance amplifier and correction of the temperature dependence of the SiPM breakdown voltage $v_{bd}(T)$. Also, the bias voltage v_b and the temperature near the SiPM have to be monitorable. This chapter aims on introducing the front-end electronics that have been developed by the author. The datasheet of the rev.F front-end electronics is attached in the appendix A.

In the last chapter we have dealt with ideal operational amplifiers (op-amps) only. Sadly, the op-amps in the real world are not *ideal*. Finite open-loop gain[1] and input impedance result in limited frequency response, i.e. *bandwidth* and *slew rate*. This will affect the small and large signal response of the op-amps dramatically. Real op-amps and resistors are sources of electronic noise. The electronic noise will smear

---

[1]The open-loop gain of an ideal op-amp is infinite which means that the differential voltage $V_D = 0$. For real op-amps $V_D \neq 0$ leading to finite open-loop gain.
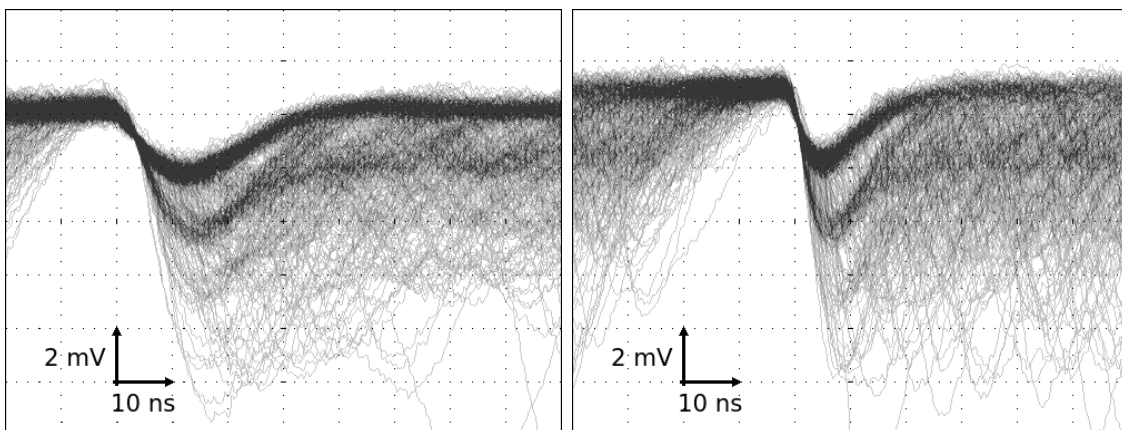
Figure 3.1: Oscilloscope screenshot of a Hamamatsu S10362-33-050C SiPM signal, amplified with the front-end electronics (rev.B) developed in this thesis. **Left**: using an Analog Devices AD8014 op-amp and **Right**: using an Intersil EL5165. Electronic noise, i.e. width of the baseline, and limited frequency response, i.e. shape of the falling edge, are clearly visible.
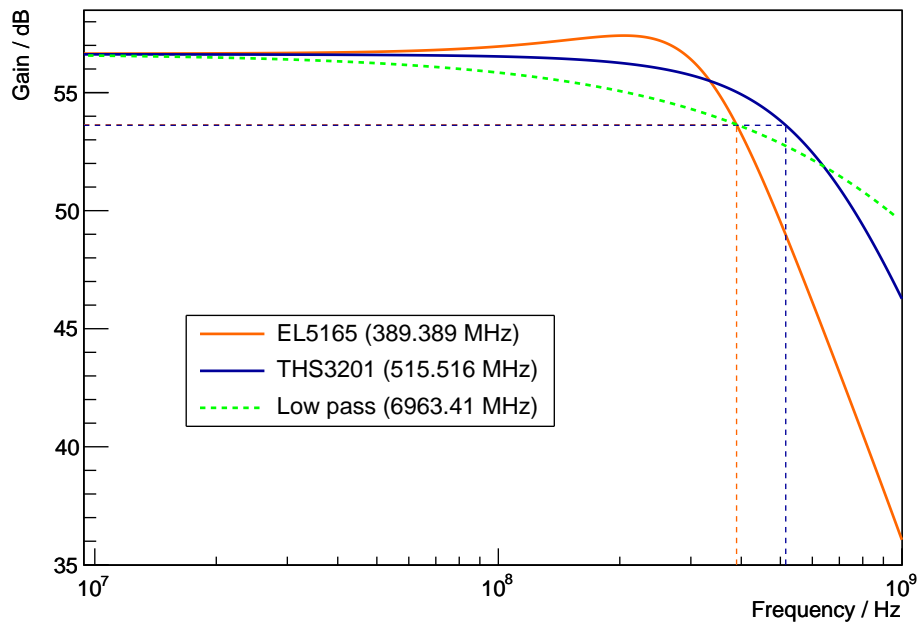
Figure 3.2: Simulated frequency response of Texas Instruments THS3201 (blue) and Intersil EL5165 (orange) configured as a transimpedance amplifier with $R_f = 680\,\Omega$. The dotted lines show the $-3\,$dB-bandwidth. In this configuration, the bandwidth of the THS3201 circuit is slightly above $500\,$MHz whereas the bandwidth of the EL5165 circuit is below $400\,$MHz. This affects the pulse response as mentioned in the text.

out the signal randomly. Figure 3.1 shows an example of an oscilloscope screenshot of the signal output of the front-end electronics developed in this thesis. Clearly, the shape of the falling edge differs from the ideal op-amp expectation calculated in the last chapter, cf. fig. 2.7. This is due to the limited bandwidth of the amplifier circuit. Also, the effects of the electronic noise of the board can be seen by the vertical fluctuations of the baseline and the resulting width of the baseline band.

To handle these effects, engineers must rely on simulations. LTspice IV, developed by Linear Technology Corporation, is a program for electronic circuit simulation based on SPICE [32]. This chapter describes the effects mentioned above by comparing theoretical expectation, simulation and measurement. First, non-ideal op-amp parameters are described and calculation methods are presented. The second part deals with the circuit layout of the front-end electronics. TARGET 3001! by Ing.-Büro Friedrich has been used for the printed circuit board (PCB) design [33].

3.1 Non-ideal operational amplifier parameters

3.1.1 Bandwidth and slew rate

The LTspice op-amp models have been developed by the manufacturers. These spice models have different levels of detail and are optimised with respect to some
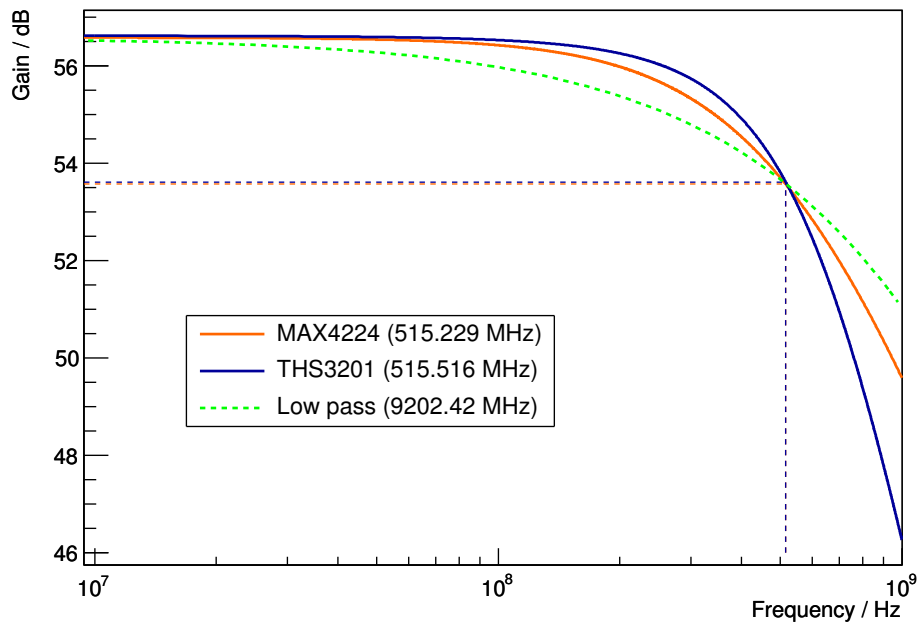
Figure 3.3: Simulated small signal gain versus frequency. $-3\,\mathrm{dB}$-bandwidths are marked for both op-amps (orange and blue). The green-dotted line shows a RC low-pass with the same $-3\,\mathrm{dB}$-bandwidth. The simulated values do not reflect the values given by the manufacturer and measured by the author due to limited op-amp model complexity, see text.

specific configuration (typically a non-inverting setting with gain 1 or 2) for better simulation performance. Detailed comparisons between the prediction of the simulations and measurements in the laboratory have been done: The simluations do not fit to the data at all. Also, the simulated op-amp responses do not agree with the specifications in the datasheets given by the manufacturers. The bandwidths of the Texas Instruments THS3201 and Maxim MAX4224 op-amps for example have been simulated in figure 3.3. Both have approximately the same simulated values of roughly 500 MHz but the parameters given by the manufacturer are up to 1800 MHz and 600 MHz, respectively [34] [35]. The op-amp response to a capacitance at the input of the inverting node of the op-amp (SiPM), as well as to the transimpedance design using a low-ohmic resistor, do not reflect the reality. The simulated plots in this chapter are therefore for demonstration purposes only.

Figure 3.2 shows the simulated frequency response of two different op-amps connected in transimpedance mode. The $-3\,\mathrm{dB}$-bandwidth $f_{-3\,\mathrm{dB}}$ is a good value to specify the frequency response of an op-amp even though it does not specify the shape of gain vs. frequency. $f_{-3\,\mathrm{dB}}$ is defined as the bandwidth between $\mathrm{DC} \equiv 0\,\mathrm{Hz}$ and the point, where the curve falls below $3\,\mathrm{dB}$ with respect to the value at DC, thus

$$f_{-3\,\mathrm{dB}} \equiv g^{-1}\left(g(\mathrm{DC}) - 3\,\mathrm{dB}\right),$$

where $g(f)$ is the frequency response of the op-amp and $g^{-1}(f) = f(g)$ its inverse. High-speed op-amps with at least $f_{-3\,\mathrm{dB}} = \mathcal{O}(\mathrm{MHz})$ have very flat frequency responses up to very high frequencies which then quickly drop to zero. From the figure above, it is obvious that the bandwidth of the circuit using the Texas Instruments THS3201 is slightly higher than the one using the Intersil EL5165. This behaviour corresponds to the bandwidths given in the datasheets by the manufacturers. The frequency response of an ideal op-amp will be completely flat. The impedance of a first order passive low-pass filter with

$$LP(f) \approx \frac{56\,\mathrm{dB}}{1 + f/9200\,\mathrm{MHz}}$$

is plotted in figure 3.2 to match the $f_{-3\,\mathrm{dB}}$ of the THS3201. Obviously, the frequency response of the op-amp does not fit exactly to a standard first order low-pass. The very steep falling edge in the SiPM signal response of an ideal op-amp calculated in the last chapter corresponds to infinitely high frequencies. This is not processable by the op-amp. For example, the time response of an RC low-pass filter on a negative unit step function is simply

$$v_o(t) = e^{-\frac{t}{RC}} - 1, \tag{3.1}$$

see fig. 3.4. This is about what we see at the falling edge in the laboratory for small SiPM signals, i.e. $M \ll N$, see figure 3.1. Op-amps with high bandwidth, i.e.

$$f_{-3\,\mathrm{dB}} \gg \frac{1}{R_q\left(C_q + C_d\right)},$$

reproduce the SiPM signal the best because the exponential fall of the low-pass becomes small. For very small bandwidths, on the other hand, the spike component τ^+ (passive) or the δ peak (active) of the SiPM signal can not be amplified reasonably. Only the slow exponential tail τ^- (passive) or $\tau = R_q(C_q + C_d)$ (active) of the signal can be seen. The main conclusion from this part is: The higher the bandwidth, the better the representation of the pulse shape.

A large pulse response can be characterised using the *slew rate* SR parameter which is usually given in units of $\mathrm{V}\mu\mathrm{s}^{-1}$ and depends on the gain. SR can be defined in various ways. Conventionally, the pulse response $v(t)$ of a unit step input is used, where
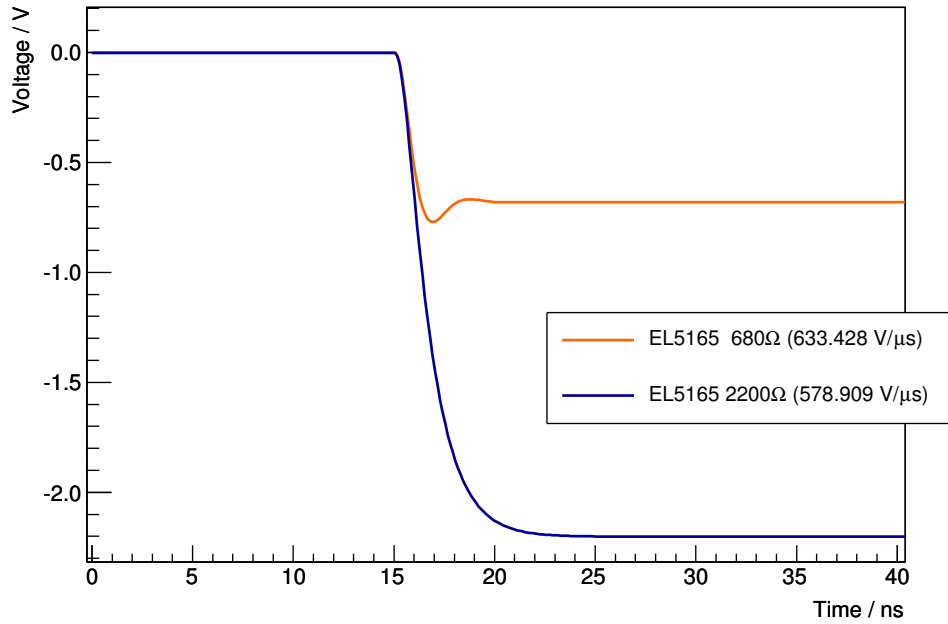
Figure 3.4: Simulated transient response of Intersil EL5165 configured as transimpedance amplifier with $R_f = 680\,\Omega$ (orange) and $R_f = 2200\,\Omega$ (blue) on a step current pulse. The falling edge corresponds to an exponential function, see eq. (3.1).

$$\text{SR} \equiv \frac{v(t_2) - v(t_1)}{t_2 - t_1},$$

and t_1, t_2 are chosen such that $v(t_1)$ and $v(t_2)$ become 10% and 90% of the pulse response maximum, respectively. For the Intersil EL5165, the simulated slew rate is somewhere around $600\,\text{V}\mu\text{s}^{-1}$, see fig. 3.4. The current input signal in this scenario is defined as

$$i(t) = 100\,\mu\text{A} \times \text{u}\,(t - 15\,\text{ns})\,,$$

where $u(t)$ is the unit step function. From figure 3.4 we know that the slew rate decreases with increasing gain in the transimpedance amplifier mode. Like the small signal response, the SR strongly depends on the op-amp type. We can conclude that op-amps with high slew rates are usually the first choice: Suppose we measure the SiPM signal within a gate window. If the SR is small, the form of large pulses will change and spread in time. The signals become wider and roam out of the gate. An asymmetry of the measurement is the result.

3.1.2 Gain

From chapter 2 we know that the gain of the signal output is directly proportional to the feedback resistor R_f, which holds at least for ideal op-amps. Increasing the
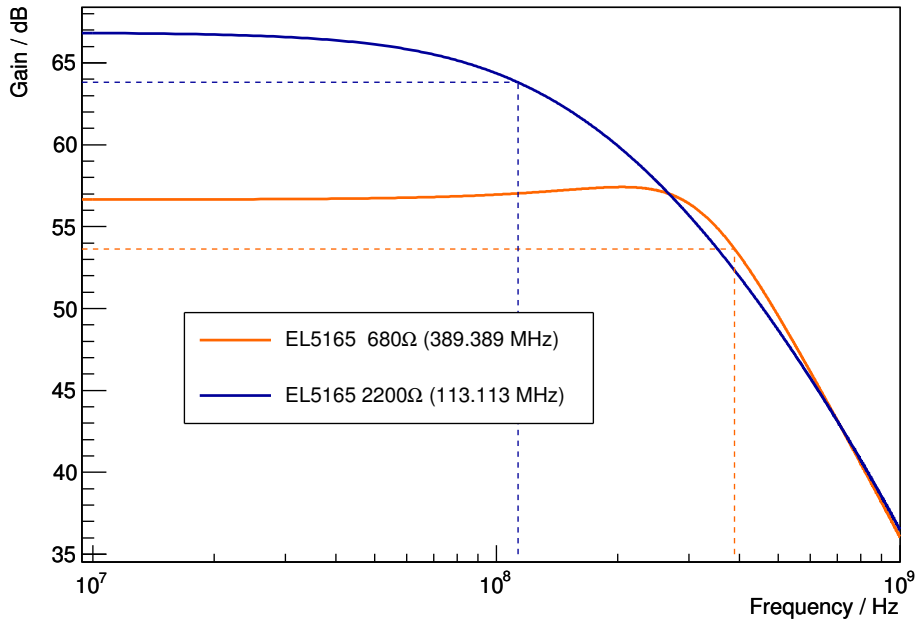
Figure 3.5: Simulated frequency response of Intersil EL5165 configured as transimpedance amplifier with $R_f = 680\,\Omega$ (orange) and $R_f = 2200\,\Omega$ (blue). The dotted lines show the $-3\,\mathrm{dB}$-bandwidth. The bandwidth $f_{-3\,\mathrm{dB}}$ decreases with increasing feedback resistance R_f. Confer with fig. 3.2.

gain results in better pulse height separation, for example separating pulses with $M = 1$ and $M = 2$ from each other. However, the bandwidth of the transimpedance amplifier suffers when using higher resistances for real op-amps. Figure 3.5 shows simulations for two different feedback resistances R_f. Due to the limited bandwidth of these op-amps, the bandwidth decreases with increasing feedback resistance as expected. The bandwidth for the Intersil EL5165 at $R_f = 680\,\Omega$ is approximately $f_{-3\,\mathrm{dB}} = 390\,\mathrm{MHz}$, whereas the bandwidth at $R_f = 2200\,\Omega$ is only $f_{-3\,\mathrm{dB}} = 113\,\mathrm{MHz}$. Reducing the gain will increase the maximal bandwidth.

3.1.3 Dynamic range

Since the maximal possible output of the op-amp is restricted by the op-amp supply voltage, which is typically $v_{S_\pm} = \pm 5\,\mathrm{V}$, a high-ohmic feedback resistor will limit the dynamic range of the SiPM, i.e. the output voltage will saturate at a light flux which is directly inversely proportional to the value of R_f. For negative output voltage $v_o < 0\,\mathrm{V}$, v_o is limited by

$$\|v_o\| \leq \|v_{S_-}\|.$$

This can be seen in figure 3.6. Here, the simulated Intersil EL5165 op-amp saturates at roughly 80% of the supply voltage $v_s = \pm 5\,\mathrm{V}$. This depends on the op-amp type, see next chapter. In this special case, the input current has been defined as
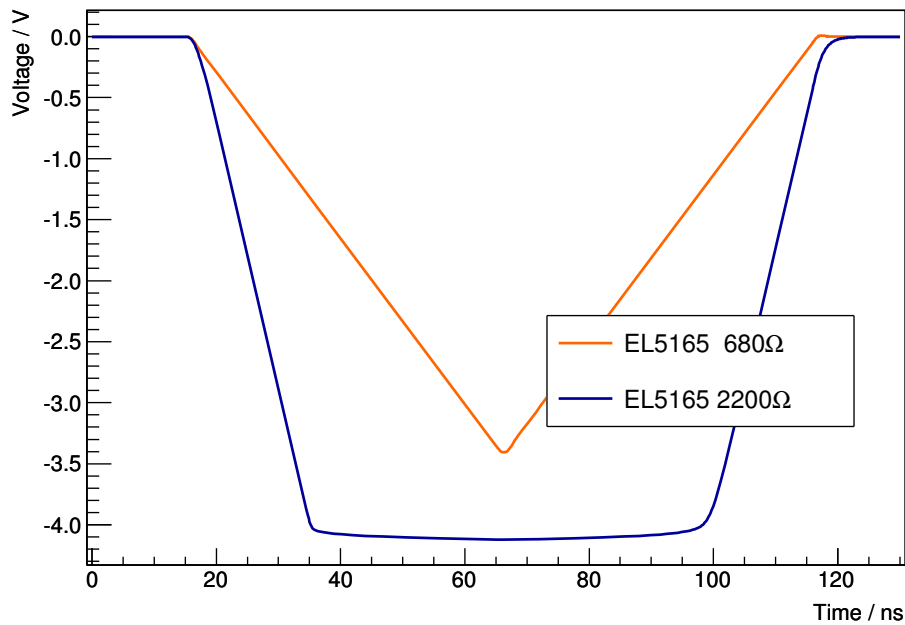
Figure 3.6: Simulated transient response of Intersil EL5165 configured as transimpedance amplifier with $R_f = 680\,\Omega$ (orange) and $R_f = 2200\,\Omega$ (blue) on a triangle current pulse. The high gain version saturates at roughly 80% of the supply voltage. The shape of the original triangle pulse for the high gain version (blue) is disturbed.

$$i(t) = 5\,\mathrm{mA} \times \mathrm{tri}\left(\frac{t - 15\,\mathrm{ns}}{50\,\mathrm{ns}}\right),$$

with $\mathrm{tri}(t)$ being the triangle function. In order to reproduce the SiPM signal even for high light levels, i.e. large current signals, the gain must be kept as low as possible.

3.1.4 Electronic noise

The noise observed at the output of an arbitrary circuit can have several causes. One part is generated internally, for example in the integrated circuits, thermally in resistors and the like. But usually, the most dominant effect comes from external sources which is received on cables for example [36]. Externally generated noise can be reduced by electro-magnetic shielding. Therefore, this chapter centers upon internal noise sources only. The noise densities of the op-amps considered in this thesis follow a superposition of pink and white noise [34] [37] [38]. Electronic noise will result in voltage fluctuations on the signal output. Pink noise is distributed like $1/f$ in the frequency spectrum, whereas white noise is flat. Thus, the pink part dominates the lower frequency range only. The transition frequency where the white noise becomes dominating is called the corner frequency f_{nc}. The color-term of noise have originally come from the analogy to light [36].

However, op-amps with high bandwidth integrate large amount of noise, from which we deduce that the bandwidth shall be kept low to avoid high electronic noise in the output. This feature depends likewise on the op-amp type. According to Friis noise formula from 1946 [39], the noise of a multi-stage amplifier is transferred to and amplified by each op-amp. A one-stage amplifier consisting only of one op-amp keeps the noise as low as possible. Also, the noise does not greatly depend on the gain [36], meaning that high-gain amplifiers have lower relative noise and therefore higher signal to noise ratios.

3.1.5   Conclusion

The conclusions of the last section are partly in contradiction with each other. For example, amplifiers using high speed op-amps will benefit from nice SiPM signal reproduction but suffer from higher integrated electronic noise. On the one hand, implementing high gain amplifiers will guarantee good pulse height separation and low relative electronic noise; on the other hand high gain amplifiers will lower the bandwidth and dynamic range.

Which type you choose depends on the area of application. The perfect op-amp configured as a transimpedance amplifier for the use in SiPM signal amplification must have a low electronic noise, medium bandwidth and high slew rate. The dynamic range of the output will benefit from a high supply voltage V_s. Depending on the field of use, the feedback resistor R_f shall be chosen such that the dynamic range is sufficient. For example, if the scientist is doing measurements with low light fluxes or even dark noise characterisations, R_f may be increased by a factor of 2 or 3. On the other hand, measurements of the dynamic range of an SiPM with a lot of cells require the feedback resistor to be kept as low as possible. When the feedback resistance becomes too low, the circuit looses stability and the output results in ringing and oscillation.

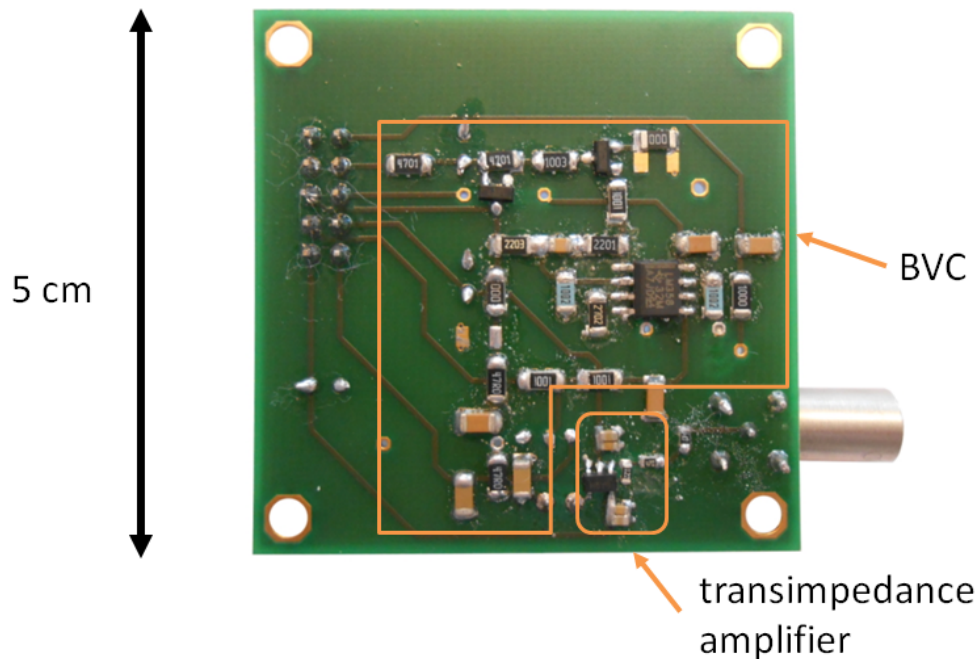## 3.2   Layout of the front-end electronics

Six revisions (rev.A - rev.F) have been developed by the author of which four revisions (rev.B, rev.C, rev.E, rev.F) have made it to the manufacturing process. Three revisions (rev.B, rev.E, rev.F) have been soldered and assembled. Rev.B has been used to test the transimpedance design. It consists of a few terminals for supply voltages, bias voltage v_b and GND, SiPM sockets and LEMO signal output. Measurements of op-amp parameters have been performed with this revision. The temperature compensation unit has been introduced with rev.E. Rev.F is the last version. The printed circuit board (PCB) has been created externally by a professional PCB manufacturer. All advantages of the previous revisions have been combined and the board offers connections for temperature and bias voltage monitoring.

Figures 3.7 and 3.8 show photos of the front-end electronics after the soldering process. The printed circuit board (PCB) is smaller than $5 \times 5\,\mathrm{cm}^2$ in size and has been manufactured by PCB-POOL, see discussion about the economic aspects in section 4.4. One of four boards has been soldered by the author of this thesis in
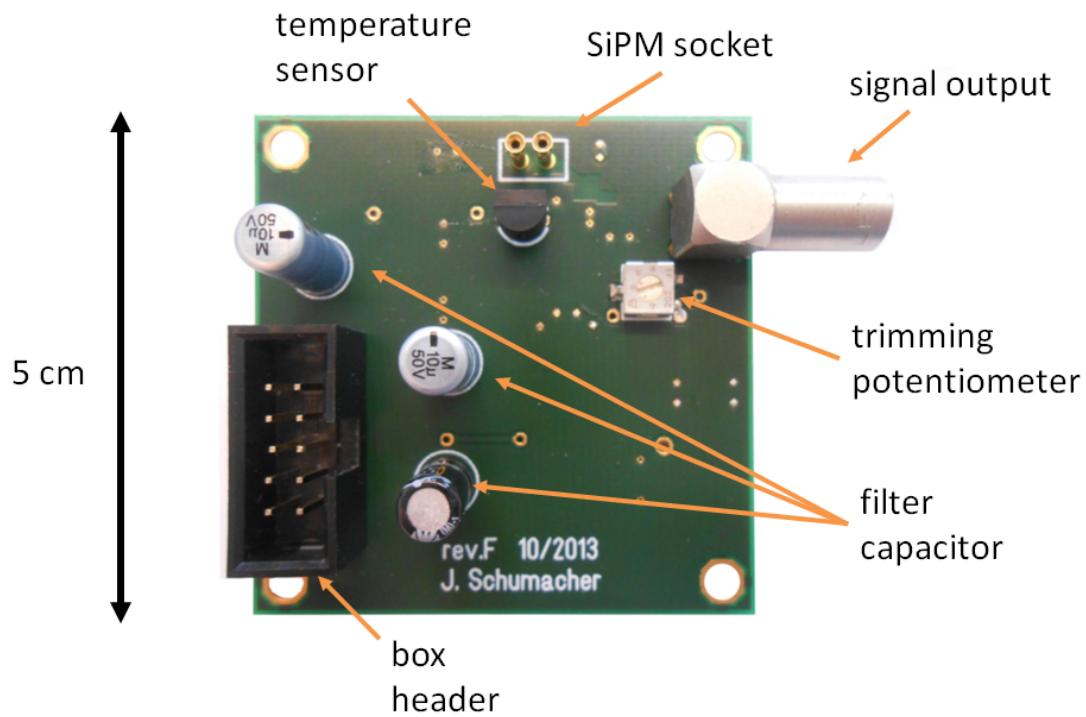
Figure 3.7: Top view of the last revision (rev.F) of the front-end electronics board after being soldered by the author. Two prototypes have been made in October 2013. The board is roughly $5 \times 5\,\text{cm}^2$ in size. Surface mounted devices (SMD), like the transimpedance amplifier, are deployed on the other side, see fig. 3.8.

Figure 3.8: Bottom view of the last revision (rev.F) of the front-end electronics board after being soldered by the author. Compare with figure 3.7. The SMD parts like the transimpedance amplifier and the BVC circuit are soldered at this side.
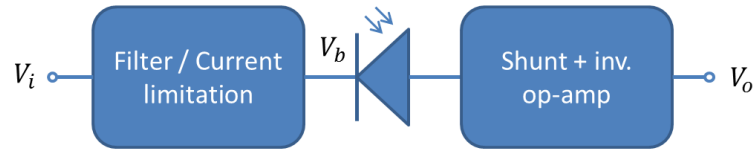
Figure 3.9: Default read-out layout proposed by SiPM manufacturers: An SiPM (represented by the photodiode symbol) read out by a shunt resistor R_s to ground and amplified with an inverting operational amplifier (op-amp). A passive RC low-pass filter is used to limit the current and to filter high frequencies from the bias voltage v_b.
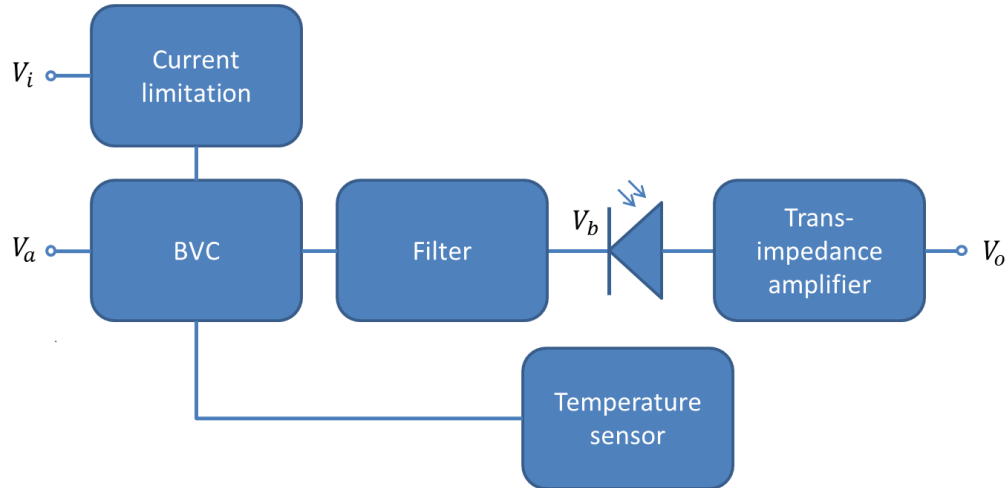
Figure 3.10: Simplified read-out layout proposed in this thesis: An SiPM (represented by the photodiode symbol) read out by a transimpedance amplifier. Passive LC low-pass filters are used to filter high frequencies from the bias voltage v_b. A transistor circuit limits the current in the SiPM and compensates the breakdown voltage temperature dependence using a temperature sensor. The full layout is printed in the appendix, see figure A.3. Details in the text.

October 2013. In this section, the circuit layout is introduced. The full layout is printed in the appendix, see fig. A.3. In figure 3.10, a schematic version is shown in order to explain why this layout is better than the default circuits proposed by the SiPM manufacturers. Details are mentioned in the following subsections.

The default layout proposed by several manufacturers [23] [22] [26] is quite easy to understand, see figure 3.9: A low-pass at the cathode of the SiPM is used to limit the current and to filter high frequencies from the constant bias voltage. The SiPM signal output has already been introduced in the last chapter and is based on a shunt resistor and an (inverting) op-amp.
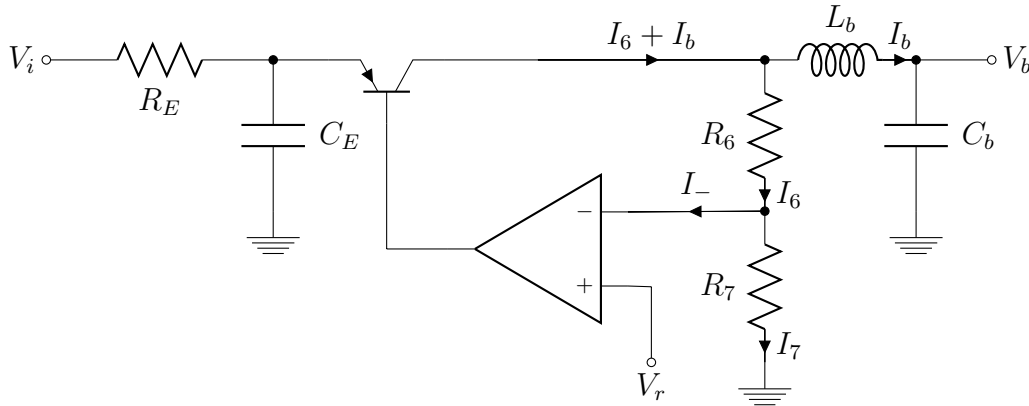
3.2.1 Beissel voltage controlling circuit

The *Beissel voltage controlling* (BVC) circuit has originally been introduced by Franz Beissel († 2012) at III. Physikalisches Institut, RWTH Aachen University. Figure 3.11 shows a very simplified version of the BVC circuit. The simplified version can be used to explain the DC performance of the voltage controller.

The differential voltage at the op-amp is zero, which means that the op-amp is trying to pull the voltage in the inverting node to V_r. A current flows through the resistor R_7 which is equal to

$$I_7 = V_r/R_7.$$

The op-amp draws no current in the input, that is $I_- = 0$. The same current I_7 flows through the resistor R_6. Therefore,

Figure 3.11: Highly simplified circuit of the *Beissel voltage controlling* circuit modified in this thesis, see fig. A.3 for detailed circuit elements. The voltage at node V_b is set by the op-amp according to eq. (3.2). This simplified circuit is valid for DC performance only and especially when no current is drawn at the V_b node, i.e. $I_b = 0$.

$$I_7 = I_6$$
$$\Leftrightarrow V_r/R_7 = (V_b - V_r)/R_6$$

and solving by the bias voltage V_b finally gives

$$V_b = (1 + R_6/R_7)\, V_r. \tag{3.2}$$

This holds only for $V_i \geq V_b$, because the transistor has to provide the circuit with enough power. For DC, the s-domain and t-domain voltages are the same. This means that the reference voltage v_r can be used to set the bias voltage to any value between $0\,\mathrm{V}$ and v_i. The full BVC circuit has additional AC performance, when the SiPM at V_b is pulling a current $I_b \neq 0$.

3.2.2 Current limitation

Many manufacturers propose a very simple front-end scheme for the use of silicon photomultipliers, e.g. [23] [22] [26]. Besides standard read-out by means of a shunt resistor and a voltage amplifier, resistors are used for both, filtering and current limitation. The next two subsections deal with improved techniques of these two necessary elements and enumerate the disadvantages of the standard approach compared with the methods proposed in this thesis. The advantage of this standard method is that it is a very simple approach and easy to be implemented since only one resistor is needed.

Silicon photomultipliers drain power from the bias voltage source. The current is directly proportional to the amount of firing cells, see chapter 2. To protect the SiPM from being thermally destroyed, the current must be limited to a reasonable value. The standard approach is shown in figure 3.12. The voltage at the SiPM will be lowered to

$$V_b = V_i - R\,I_{\mathrm{SiPM}}, \tag{3.3}$$

with V_i being the input voltage on the one side of the resistor which is assumed to be constant. Once the bias voltage V_b is smaller than the breakdown voltage V_{bd}, the SiPM will stop drawing a current, i.e. I_{SiPM} becomes 0 such that

$$I_{\mathrm{max}} = \frac{V_i - V_{\mathrm{bd}}}{R}. \tag{3.4}$$

This effect has serious consequences. When the SiPM draws a current I_{SiPM} less than I_{max}, the bias voltage V_b will decrease to the value specified by eq. (3.3). But this
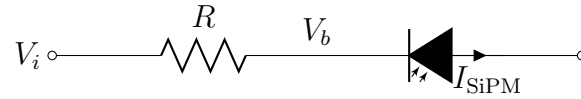
Figure 3.12: Standard approach to limit the current I drawn by an SiPM (represented by a photodiode symbol here). The voltage drop at the resistor created by the current will lower the bias voltage at the SiPM to $V_b = V_i - R\,I$.

means that the overvoltage $V_{\mathrm{ov}} = V_b - V_{\mathrm{bd}}$ will decrease by the same amount, too. As already mentioned in chapter 2, the overvoltage is probably the most important parameter of the SiPM on which a lot of values depend, e.g. gain, photon detection efficiency (PDE) and correlated noise effects. If the SiPM is illuminated with a large amount of light[2], the overvoltage of the SiPM will change dramatically. This, however, depends linearly on the resistance of the current limiting resistor. One way to overcome this effect is therefore to reduce the resistance. But first, this method will only reduce (not eliminate) the voltage drop and secondly, the current limitation effect decreases. Remember that we have taken V_i to be constant.

The current limitation method proposed in this thesis is based on a very simple way. Instead of applying the supply voltage for the SiPM V_i to a current limiting resistor R_E, the current is limited before and the supply voltage for the SiPM is adjusted afterwards. This approach has been implemented with the voltage controller circuit, see figure 3.11. The op-amp in this circuit will regulate the voltage at the inverting node such that the voltage at the SiPM is constant. The necessary power for the voltage divider comes from the PNP transistor. The resistor at the emitter of the transistor limits the current. Since the voltage at the collector V_C of the transistor will always be smaller or equal to the supply voltage at the emitter $V_E \geq V_C$, the maximal current will also be defined by equation (3.4). However, this only holds for ideal components (transistors, op-amps and so on). Especially for pulsed DC analyses, i.e. current pulses, or even AC, this technique has limitations. The capacitor at the emitter of the PNP is used for filtering and to supply power for small and short current pulses drawn by the SiPM.

Another method, which is also based on the standard approach, is simply to measure the current I_{SiPM} that is drawn by the SiPM. Knowing the current limiting resistance R and I_{SiPM} will allow the researcher to calculate the real bias voltage at the SiPM according to formula (3.3). This can be realised by using an ammeter. Strictly speaking, the voltage drop will not be prevented, but the effect on the overvoltage will be known.

3.2.3   Filter

Usually, one or more RC low-pass filters are used to suppress any frequencies in the supply voltage of the SiPM, see figure 3.13. Since the current through the resistor and through the capacitor are the same, which holds for an unloaded low-pass filter, i.e. $I_o = 0$, it is quite easy to calculate the output voltage in the s-domain

---

[2]"large amount" means that the voltage drop posed in equation (3.3) becomes significant.
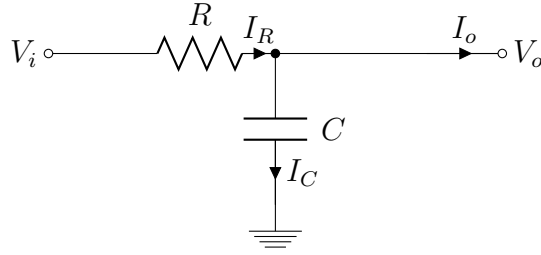
Figure 3.13: This circuit is a standard RC low-pass filter which is used to filter any frequencies in the output voltage V_o from the input voltage V_i. If the filter is unloaded, i.e. $I_o = 0$, this filter will suppress the gain according to equation (3.5) in the s-domain. For $I_o \neq 0$, V_i in eq. (3.5) must be replaced by $V_i - RI_o$.
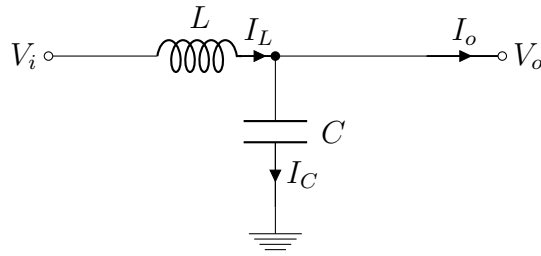
Figure 3.14: Ideal circuit of a LC low-pass filter, cf. fig. 3.13. For an unloaded filter, i.e. $I_o = 0$, eq. (3.6) holds. This filtering technique eliminates the voltage drop in the case of ideal elements.

$$V_o = \frac{V_i}{1 + sRC}. \tag{3.5}$$

To suppress even very low frequencies, RC must be as high as possible or multiple RC filters must be used in series. Increasing the resistance R however, will result in the problem discussed earlier, see previous section. The bias voltage at the SiPM will decrease linearly with RI, see again eq. (3.3). To avoid this problem in this thesis, inductors have been chosen instead of resistors. A LC low-pass filter will work very similarly, see figure 3.14. Applying the same calculations like above gives

$$V_o = \frac{V_i}{1 + s^2 LC}. \tag{3.6}$$

Although filtering is quadratic in s, LC low-pass filters are not very effective, since the inductors used in this thesis are very small $L < 1\,\mu\text{H}$. Therefore, a standard RC low-pass filter has been integrated before the BVC and multiple LC filters have been used in series after the BVC. For an ideal inductor, no voltage drops at L which means that LC filters can be implemented right before the SiPM without the problem of voltage drops discussed earlier. However, inductors are not perfect. In fact, they have a small equivalent series resistance R_{ESL} usually less than $1\,\Omega$ for DC.

The series resistance of the inductors used in the test boards is smaller than $0.7\,\Omega$ each. Therefore, a pin has been reserved for revision F allowing the researcher to measure the current through the inductors at any time. A small resistance is even necessary to reduce the risk of oscillation. But, compared to the standard methods which propose several $k\Omega$ resistors, the voltage drop for revision F is negligible, because a naïve fallacy shows that the maximal voltage drop is

$$
\begin{aligned}
V_{\mathrm{max}} &= R_{\mathrm{ESL}} I_{\mathrm{max}} \\
&\stackrel{(3.4)}{=} \frac{R_{\mathrm{ESL}}}{R_E} \left(V_i - V_{\mathrm{bd}} \right),
\end{aligned}
\tag{3.7}
$$

with R_E being the resistor at the emitter of the NPN transistor and eq. (3.4) has been used. Since $R_{\mathrm{ESL}} = \mathcal{O}(\Omega)$, $R = \mathcal{O}(k\Omega)$ and $v_i - v_{\mathrm{bd}} = \mathcal{O}(V)$, the maximal voltage drop is therefore

$$
v_{\mathrm{max}} = \mathcal{O}(\mathrm{mV})
$$

at most. When V_i drops below the desired bias voltage V_b at the SiPM configured via the adjust voltage V_a, the bias voltage will decrease, too. This happens when the following equation holds

$$
\begin{aligned}
I_{\mathrm{drop}} &= \frac{V_i - V_b}{R_E} \\
&\leq I_{\mathrm{max}},
\end{aligned}
$$

where R_E again is the resistance at the emitter of the NPN transistor, meaning that no voltage drops at the SiPM, except for $R_{\mathrm{ESL}} I$, until the current drawn by the SiPM reaches I_{drop}. For the current configuration of revision F, with $R_E = 4.7 k\Omega$, $v_i = 80\,\mathrm{V}$ and $v_b \approx 70\,\mathrm{V}$ for typical Hamamatsu SiPMs, the current becomes $i_{\mathrm{drop}} \approx 2\,\mathrm{mA}$. Revision F comes in two different versions. The first one has high gain which is the perfect choice for low light level measurements; the other one has low gain which offers a higher dynamic range. The low gain version also has smaller resistance at the emitter of the NPN transistor allowing the SiPM to draw higher currents, confer equation (3.4).

3.2.4 Temperature compensation

In the previous chapters, we have already seen how the voltage controller works. Based on these results, we can now introduce the temperature compensation unit, which will eliminate the temperature dependence of the breakdown voltage of the SiPM. In this section we assume that currents and voltages are constant in time, that is $V \Leftrightarrow v$. Remember that the breakdown voltage
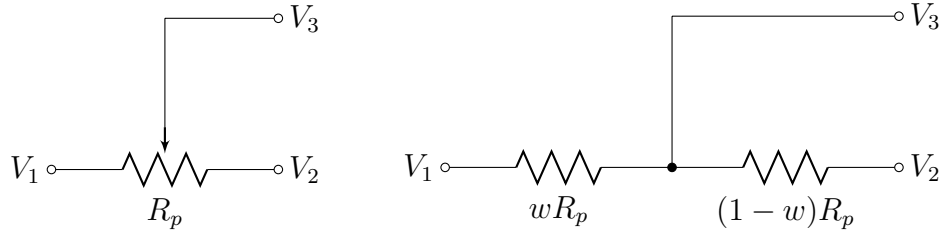
Figure 3.15: Left: A trimming potentiometer (trimpot) **Right**: Equivalent circuit of an ideal trimpot. The ratio w between the two resistors can be adjusted by turning the screw either clockwise of counter-clockwise. Basic voltage divider rules apply.
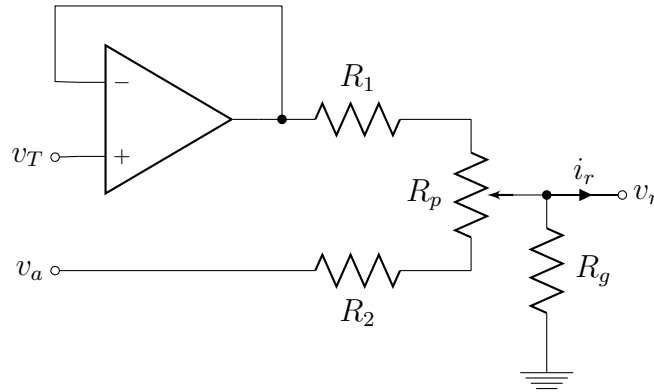
Figure 3.16: Simplified circuit diagram of the temperature compensation circuit. v_T is the voltage output of a linear temperature sensor, see eq. (3.9). An impedance converting op-amp is used to allow driving loads that are not connected to ground. The adjust voltage v_a and the wiper wR_p must be set according to the parameterisations from eq. (3.12). The reference voltage v_r is fed to the non-inverting input node of the op-amp of the voltage controller, see previous sections.

$$v_{\text{bd}}(T) = v_{\text{bd}}(T_0) + \beta \left(T - T_0\right)$$

increases linearly with temperature T. Also, β is usually between $0\,\text{mV}\,^\circ\text{C}^{-1}$ and $100\,\text{mV}\,^\circ\text{C}^{-1}$. We will come back to this later. To adjust β at the front-end electronics directly, a trimming potentiometer (trimpot) is chosen. A trimpot has three connections, see figure 3.15b. By turning the screw, one is able to vary the ratio between the two resistors, which is denoted as w in the figure above. One end is connected to the adjust voltage v_a, see figure 3.16. The output of the temperature sensor is connected to an impedance converter first. This allows the sensor to drive loads that are not connected to ground but even to higher potentials. The output of the impedance converting op-amp is applied to the other end of the trimpot. The wiper node v_r at the trimpot is connected to the non-inverting input of the op-amp of the voltage controller circuit, see previous sections. From figure 3.16 and from the fact that (ideal) op-amps draw no current at the input nodes such that the current at node v_r is zero $i_r = 0$, one gets

$$\frac{v_T - v_r}{R_1 + wR_p} + \frac{v_a - v_r}{R_2 + (1 - w)R_p} = \frac{v_r}{R_g}, \tag{3.8}$$

where

$$v_T(T) = v_T(T_0) + \alpha(T - T_0) \tag{3.9}$$

is the voltage output of a linear temperature sensor. From the previous chapter, we know that the voltage at the output of the voltage controller is

$$v_b = (1 + R_6/R_7)\, v_r,$$

cf. eq. (3.2). Inserting all the equations from this chapter into eq. (3.8), using $v_b = v_{bd}(T) + v_{ov}$, $T_0 \equiv 0\,°\text{C}$ and sorting by orders of T finally gives

$$\frac{v_T(0\,°\text{C})}{R_1 + wR_p} + \frac{v_a}{R_2 + (1 - w)R_p} + \frac{\alpha T}{R_1 + wR_p}$$
$$= \left(\frac{1}{R_1 + wR_p} + \frac{1}{R_2 + (1 - w)R_p} + \frac{1}{R_g}\right)\left(\frac{v_{bd}(0\,°\text{C}) + v_{ov}}{1 + R_6/R_7} + \frac{\beta T}{1 + R_6/R_7}\right).$$

To eliminate the temperature dependence of the breakdown voltage, the following equations must hold

$$\frac{v_T(0\,°\text{C})}{R_1 + wR_p} + \frac{v_a}{R_2 + (1 - w)R_p}$$
$$= \left(\frac{1}{R_1 + wR_p} + \frac{1}{R_2 + (1 - w)R_p} + \frac{1}{R_g}\right)\frac{v_{bd}(0\,°\text{C}) + v_{ov}}{1 + R_6/R_7} \tag{3.10}$$
$$\frac{\alpha}{R_1 + wR_p} = \left(\frac{1}{R_1 + wR_p} + \frac{1}{R_2 + (1 - w)R_p} + \frac{1}{R_g}\right)\frac{\beta}{1 + R_6/R_7}. \tag{3.11}$$

Solving eq. (3.10) for the adjust voltage v_a and eq. (3.11) for the trimming potentiometer ratio w gives quite complicated equations, and will not be printed at this point for reasons of better readability, see eq. (A.13) and (A.14) for details. The exact solutions are plotted in fig. 3.17 and fig. 3.18 using the parameters for rev.F. One can see that β can be selected freely from $10\,\text{mV}\,°\text{C}^{-1}$ to $85\,\text{mV}\,°\text{C}^{-1}$. For larger or smaller β, the resistors on the board have to be changed according to
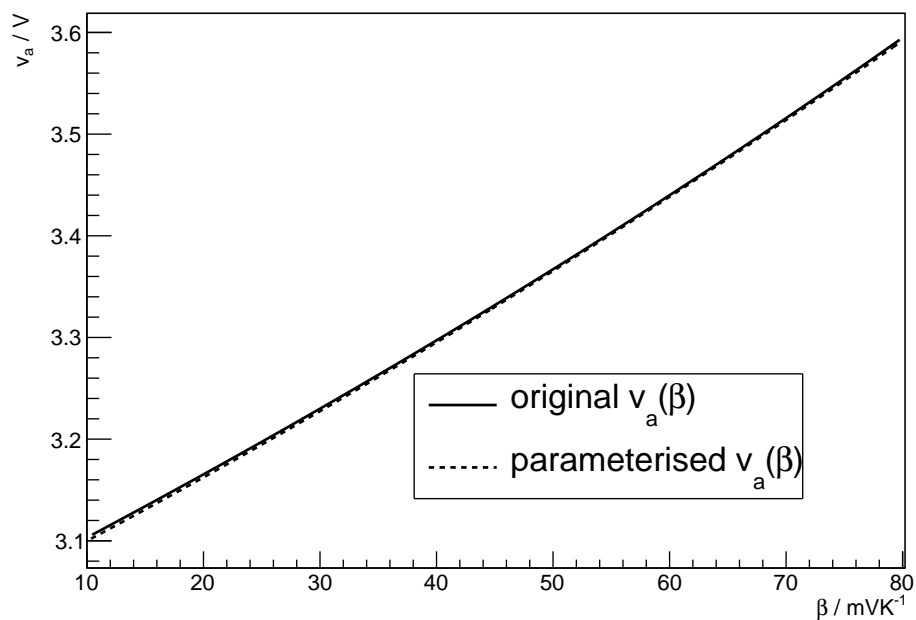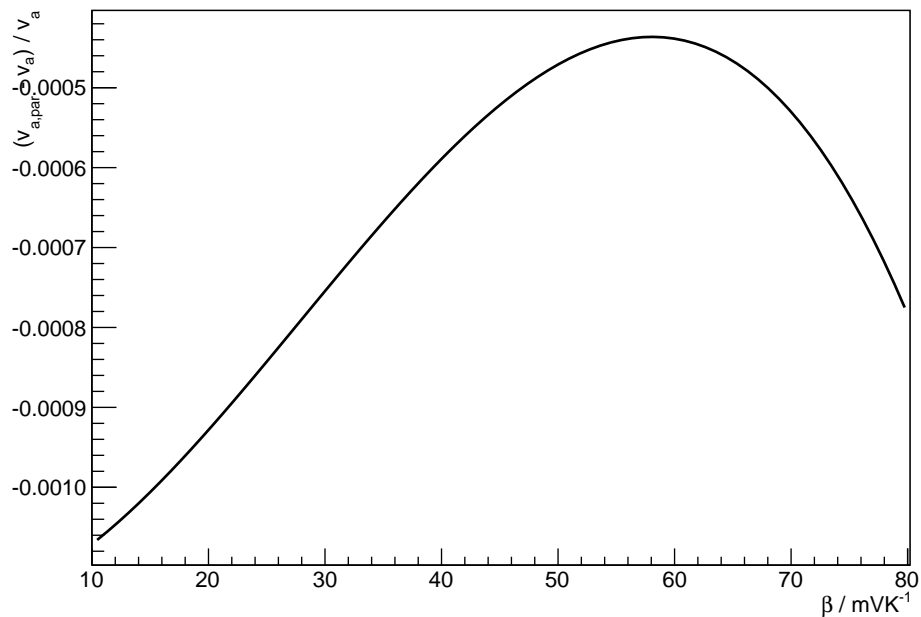
Figure 3.17: Adjust voltage v_a versus SiPM temperature coefficient β. β is typically between $10\,\mathrm{mV}\,°\mathrm{C}^{-1}$ and $100\,\mathrm{mV}\,°\mathrm{C}^{-1}$. $v_{\mathrm{bd}}(0\,°\mathrm{C}) + v_{\mathrm{ov}} = 70\,\mathrm{V}$ is used here. Compare with fig. 3.18. Parameterised function taken from eq. (3.12).
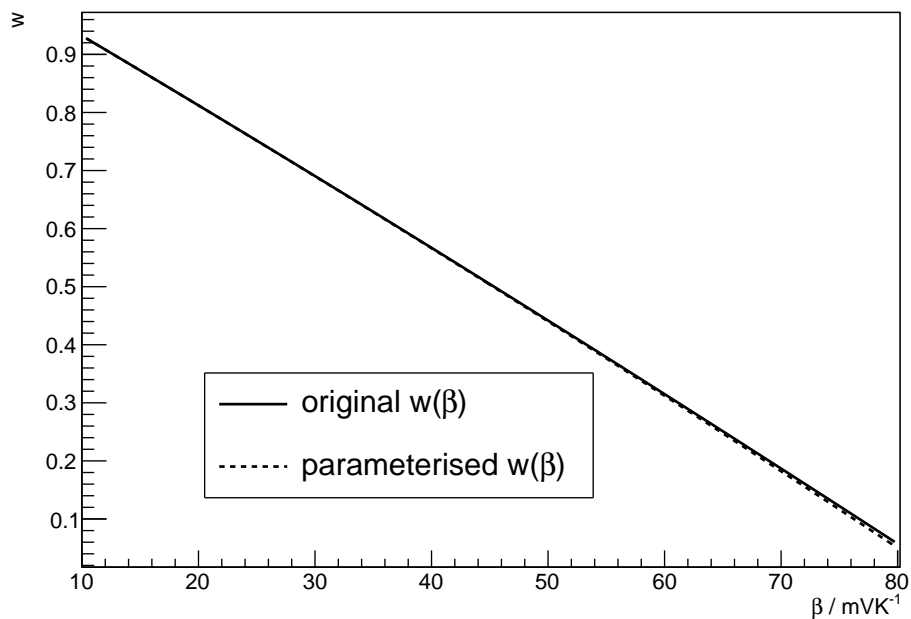
Figure 3.18: Trimming potentiometer parameter w versus SiPM temperature coefficient β. β is typically between $10\,\mathrm{mV}\,°\mathrm{C}^{-1}$ and $100\,\mathrm{mV}\,°\mathrm{C}^{-1}$. Compare with fig. 3.17. Parameterised function taken from eq. (3.12) for any v_b.
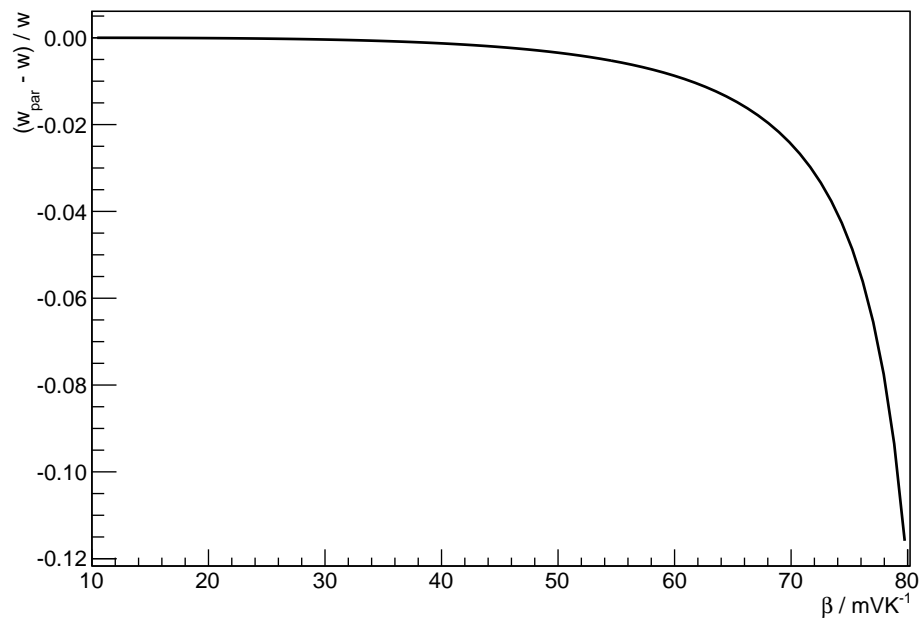
Figure 3.19: Relative difference between parameterised trimming potentiometer parameter w_{par} from eq. (3.12) and exact formula w versus SiPM temperature coefficient β. β is typically between $10\,\text{mV}\,^\circ\text{C}^{-1}$ and $100\,\text{mV}\,^\circ\text{C}^{-1}$.

Figure 3.20: Relative difference between parameterised adjust voltage $v_{\text{a,par}}$ from eq. (3.12) and exact formula v_a versus SiPM temperature coefficient β. β is typically between $10\,\text{mV}\,^\circ\text{C}^{-1}$ and $100\,\text{mV}\,^\circ\text{C}^{-1}$.

Table 3.1: Typical temperature controller adjust voltage and resulting bias voltage at room temperature ($T \equiv 25\,°\mathrm{C}$) and $\beta = 56\,\mathrm{mV°C^{-1}}$

v_a / V	v_b / V	v_a / V	v_b / V
3.30	69.24	3.40	71.20
3.32	69.63	3.42	71.59
3.34	70.03	3.44	71.98
3.36	70.41	3.46	72.37
3.38	70.81	3.48	72.76

the equations above. Plugging in the values which have been selected for revision F of the front-end electronics, these equations can be parameterised as

$$
\begin{aligned}
w(\beta) &\approx w_0 + w_1 \frac{\beta}{100\,\mathrm{mV°C^{-1}}} + w_2 \left(\frac{\beta}{100\,\mathrm{mV°C^{-1}}} \right)^2 \\
v_a(\beta) &\approx v_0 + v_1 \frac{\beta}{100\,\mathrm{mV°C^{-1}}} + v_2 \left(\frac{\beta}{100\,\mathrm{mV°C^{-1}}} \right)^2,
\end{aligned}
\tag{3.12}
$$

with

$$
\begin{aligned}
w_0 &= 1.050 \\
w_1 &= -1.169 \\
w_2 &= -0.101 \\
v_0 &= 0.043 \left(v_{\mathrm{bd}}(0\,°\mathrm{C}) + v_{\mathrm{ov}} \right) \\
v_1 &= 0.012 \left(v_{\mathrm{bd}}(0\,°\mathrm{C}) + v_{\mathrm{ov}} \right) - 0.266\,\mathrm{V} \\
v_2 &= 0.003 \left(v_{\mathrm{bd}}(0\,°\mathrm{C}) + v_{\mathrm{ov}} \right) - 0.074\,\mathrm{V}.
\end{aligned}
\tag{3.13}
$$

Table 3.1 may help to find the desired adjust voltage v_a. For typical Hamamatsu SiPMs with $\beta = 56\,\mathrm{mV°C^{-1}}$, the parameters become

$$
w(56\,\mathrm{mV°C^{-1}}) = 0.366
\tag{3.14}
$$

$$
v_a(56\,\mathrm{mV°C^{-1}}) = 0.051 \left(v_{\mathrm{bd}}(0\,°\mathrm{C}) + v_{\mathrm{ov}} \right) - 0.175\,\mathrm{V}.
\tag{3.15}
$$

Figures 3.19 and 3.20 show the relative difference between the parameterised equations from eq. (3.12) and the exact solutions. For high values of β, the parameterisation of w becomes invalid. For small values, however, the approximation is better than 2%. The parameterisation of v_a peaks around $60\,\mathrm{mV°C^{-1}}$ and loses significance for small and high values of β. In the laboratory, the monitor ports of the front-end board shall be used to measure the bias voltage at the SiPM and to select the perfect setting.
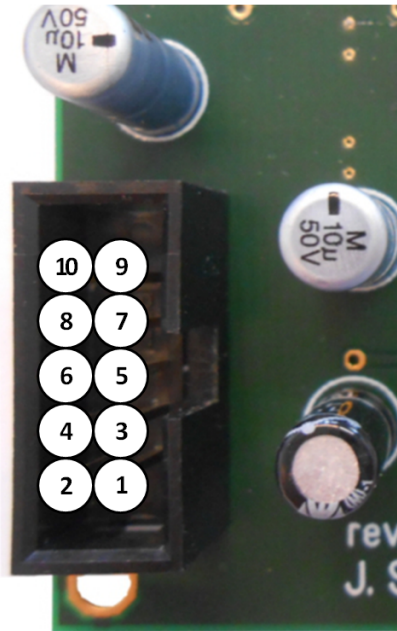
Figure 3.21: This image shows a zoom on the box header of rev.F. The pin layout is described in table 3.2.

Table 3.2: Pin layout of the front-end electronics rev.F

Pin	Node	Typical conf.	Pin	Node	Typical conf.
10	v_{S_+}	+5 V	9	v_+	+5 V
8	v_T (mon.)	-	7	v_{S_-}	−5 V
6	v_{bias} (mon.)	-	5	v_{C_+}	+5 V
4	GND	GND	3	v_i	+80 V
2	GND	GND	1	v_a	$+3.3\,\text{V} \cdots +3.5\,\text{V}$

3.3   Board layout

3.3.1   Pin layout

Table 3.2 shows the layout of the *box header* connected at the top side of the front-end board, see photo in figure 3.21. Pins 2, 4, 5, 7, 9 and 10 are reserved for supply voltages of the integrated circuits (ICs). v_{C_+} (pin 5) is the single-supply voltage of the BVC op-amp and shall be set to +5 V or at least greater than the adjust voltage v_a. $v_{S_\pm}$ are supply voltages for the + and − supply pins of the transimpedance amplifier, respectively. Usually, ±5 V is used here but the Texas Instruments THS3201 op-amp can be powered with higher voltages. Also, the supply voltage does not have to be balanced symmetrically. For example, it can be set to +3 V and −7 V, as long as $v_{S_+} - v_{S_-} \leq 10\,\text{V}$ and $\text{GND} \equiv 0\,\text{V} \in [v_{S_-}, v_{S_+}]$. Since the temperature sensor output is sensitive to the supply voltage, v_+ must be set to +5 V very accurately [40]. Pin 6 and 8 are monitor pins only. There must not be applied any voltage at these nodes!

The bias voltage (before the filter circuit, see above) can be monitored at pin 6. The temperature can be read-out at pin 8 and interpreted by using the formula

$$T/^{\circ}\mathrm{C} = \frac{v_T - 1.375\,\mathrm{V}}{22.5\,\mathrm{mV}} \tag{3.16}$$

when using the Analog Devices AD22100 temperature sensor [40] and $v_+ \equiv +5\,\mathrm{V}$, see eq. (3.9). v_i (pin 3) must be set to a value greater than the desired bias voltage v_b. For example: A typical Hamamatsu SiPM has a breakdown voltage somewhere around 70 V. Adding the overvoltage of one or two volts and taking the temperature dependence into account plus some buffer, the node must thus be connected to roughly 80 V. This value does not have to be accurate. The maximum is 100 V because of the filter capacitors which are limited to this voltage. If these devices are replaced by other capacitors which can handle higher voltages, the maximal voltage will be defined by the collector-base voltage of the NPN transistor, which is 125 V. Pin 3 is used to set the adjust voltage v_a. Parameterised equations are printed in eq. (3.12) and table 3.1.

3.3.2 SiPM socket

In figure 3.7, the top view of the soldered front-end board is shown. The SiPM socket is on the very top edge of that board (two pin connection). This allows to either set the SiPM vertically on the board, so that the sensitive area of the SiPM points directly to the viewer, or parallel by soldering angled sockets. This is quite useful, because the SiPM can be operated with minimum space requirements in several measurement setups. The transimpedance amplifier is located right next to the SiPM granting minimal target for external noise sources, see photo in fig. 3.8. The printed circuit board traces are kept small and short to minimise capacitances at this point. Also, the feedback resistor R_f is literally close to the op-amp. The resistor package of R_f is 0603 SMD meaning that its size is $6/100\,\mathrm{in} \times 3/100\,\mathrm{in}$ (less than $1.2\,\mathrm{mm}^2$). This is quite challenging to be soldered but an essential and necessary choice. The output of the op-amp is connected to two 0603 connections in series. The first one is reserved for a capacitor. A $0\,\Omega$ resistor is soldered instead by default. The capacitor can be used to eliminate DC voltage offsets. A $51\,\Omega$ resistor is connected at the second 0603 terminal providing a $51\,\Omega$ output. From here on, the trace width is doubled because the node is free of any ICs which might be sensitive to capacitances. The widened path increases the wave impedance, too. A LEMO-00 angled socket is connected at the output node. Any 00 LEMO cable can be used to monitor the output.

3.3.3 Temperature circuit

The Analog Devices AD22100 temperature sensor is located right next to the SiPM. This guarantees that the temperature measured by the sensor is nearly the same as seen by the SiPM. Any linear temperature sensor can be used instead. But they must be available as a 3-Lead TO-92 package with the same pin layout as the AD22100.

The temperature sensor output can be monitored at pin 8, see table 3.2 above. An impedance converting op-amp is used to drive the load at the output. Here, the second channel of the BVC op-amp package is used, see next subsection.

3.3.4 Beissel voltage controlling circuit

The *Beissel voltage controlling* (BVC) circuit, has been implemented here using the Infineon BCX41 (NPN) and BCX42 (PNP) SMD transistors. These ICs provide collector-emitter and collector-base voltages of up to 125 V. Thus, only SiPMs with bias voltages less than 125 V can be handled by the transistors.

A two-channel op-amp is used for the BVC-amplifier. The second channel is reserved for the impedance converting op-amp of the temperature circuit, see above. Texas Instrument's LM358 has been chosen by the author. Any other two-channel op-amp which is available in SOIC-8 providing the same pin layout can be used instead. But the LM358 is a widely used, well known and low-priced op-amp. If the reader considers to use another op-amp, here are some important facts: The op-amp must handle voltages around 3 V with high precision. The bandwidth shall be kept as low as possible to avoid unwanted noise and ringing or oscillations. The unity-gain (Gain of +1) bandwidth of LM358 is below 1 MHz. The feedback capacitor must be set according to the bandwidth of this op-amp. The higher the bandwidth, the higher the capacitance. A 2.2 nF capacitor is installed per default. Otherwise, the output in node V_b performs a sawtooth signal. The full layout and the standard values are printed in the appendix, fig. A.3.

3.3.5 Conclusion

The features of the front-end electronics have been introduced. Simulations and analytical calculations show that this layout has a lot of advantages compared to the default layout proposed by the SiPM manufacturers. We are able to filter the bias voltage, limit the current drawn by the SiPM to reduce the risk of it to be thermally destroyed, compensate the temperature dependence of the breakdown voltage and make use of the full dynamic range of the SiPM. However, these features have to be proven experimentally.

4. Characterisation of the front-end electronics

This chapter aims on experimentally proving the features of the front-end electronics that have been introduced in the last chapter. Also, characterisations of the SiPM signal response and amplifier noise are being discussed. At the end of this chapter, economic aspects, that are costs and the like, are being summarised.

4.1   Op-amp performance

In the last chapter and especially in fig. 3.1, the amplifier response to SiPM current pulses have been discussed. In this thesis, seven different op-amps have been chosen. Each of them satisfies the following conditions

- Current feedback op-amp[1]

- High slew rate

- Low input current noise density and input voltage noise density[2]

- Available in package SOT23/5.

The op-amp parameters have been simulated using LTspice and are printed in table 4.1. In table 4.2, the measured quantities are shown. The limited op-amp model performance has already been mentioned in chapter 3: Op-amp models developed for spice are usually optimised for the case of a non-inverting setting and not on low-ohmic transimpedance amplifiers with capacitances at the input and short current pulses. Comparing the results of the op-amp simulations quantitively gives no satisfactory answer. Therefore, this chapter mainly relies on measurements of the author and on the results of the manufacturer, published in the datasheets. For the simulation, a non-inverting configuration is used in order to allow at least a qualitative comparison between the simulated op-amps and a relative comparison with the measured data, see figure 4.1. The non-inverting setting uses a gain of $+2$ where the

---

[1]The inverting input node of a current feedback op-amp is low-ohmic which makes the op-amp feedback sensitive to current and provides a faster response.

[2]Input voltage and current noise densities are the voltage and current fluctuations at the input of an op-amp and usually given in units of $\mathrm{nVHz}^{-1/2}$ and $\mathrm{pAHz}^{-1/2}$, respectively, and depend on the frequency, see section about electronic noise 4.1.5 in this chapter.
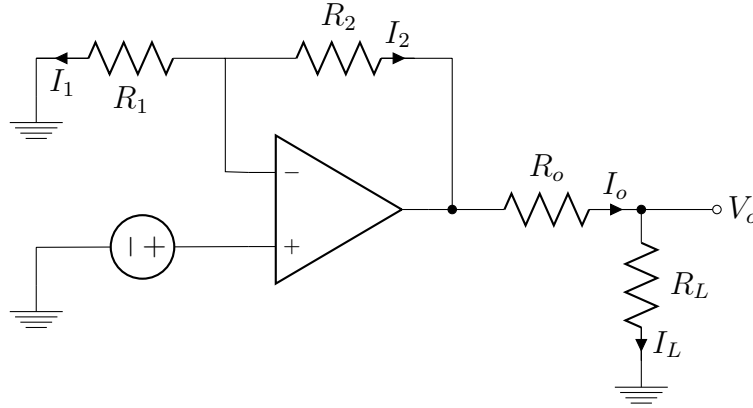
Figure 4.1: Circuit used for simulation purposes of op-amp response featuring a non-inverting amplifier, a voltage input source, output impedance R_o and loaded with resistance R_i. Feedback and output capacitance have been included in the simulation, too (not shown in this figure). SPICE op-amp models are usually optimised for this setting.

two resistors in the feedback path are both $R_1 = R_2 = 680\,\Omega$. The output is taken at a $R_L = 50\,\Omega$ load. $R_o = 50\,\Omega$ is chosen, as implemented in the front-end electronics. An input voltage pulse from $+2.5\,\mathrm{V}$ to $-2.5\,\mathrm{V}$ is placed at the non-inverting input node, i.e.

$$v_-(t) = 2.5\,\mathrm{V} - 5.0\,\mathrm{V}\,u(t),$$

where $u(t)$ denotes the Heaviside function. Applying Kirchhoff's laws yields the output voltage $v_o(t) = v_-(t)$ for an ideal op-amp. To make this scenario more realistic, the slew rate of this pulse has been set to roughly $1700\,\mathrm{V}\mu\mathrm{s}^{-1}$ which corresponds to

Table 4.1: Simulated op-amp parameters for $G = +2$

Op-amp	Bandwidth / MHz	Slew rate / $\mathrm{V}\mu\mathrm{s}^{-1}$	v_{sat} / V
AD8014	120	1046	-1.55
EL5165	298	1202	-1.81
MAX4224	387	646	-1.58
THS3201	679	1139	-1.92

Table 4.2: Measured op-amp parameters for $R_f = 680\,\Omega$

| Op-amp	Slew rate* / $\mathrm{V}\mu\mathrm{s}^{-1}$	v_{sat} / V
AD8014	330	-1.75
EL5165	311	-1.82
MAX4224	200	-1.52
THS3201	297	-1.72

the LED flash signal used in the measurement setup. Parasitic capacitances at the resistors and the solder joints have been implemented. This will guarantee a good basis for comparisons.

Texas Instrument's THS3201 offers the highest bandwidth and one of the highest slew rates of the tested op-amps. This op-amp saturates at $-1.92\,\text{V}$ (simulated). Another advantage of this op-amp is the fact that the supply voltage $V_s = V_{s_+} - V_{s_-}$ can be increased to $15\,\text{V}$, that is $V_{s_\pm} = \pm 7.5\,\text{V}$, according to the datasheet [34]. This increases the dynamic range of the op-amp by roughly 50%. The following subsections deal with detailed measurements of the op-amp response.

4.1.1 Gain

In this work, the gain of the rev.B amplifier boards has been measured in detail using an SiPM as a current source and an oscilloscope for displaying the output of the amplifiers. The gain of a transimpedance amplifier can be varied by changing the feedback resistance R_f. This has already been derived in eq. (2.22) on page 23. The first prototypes have been equipped with $R_f = 680\,\Omega$ 0603 SMD resistors. The maximum of the 1 p.e. peak of a $3 \times 3\,\text{mm}^2$ Hamamatsu SiPM S01362-33-050C at a $50\,\Omega$ load (oscilloscope) is between $-2.4\,\text{mV}$ and $-3.6\,\text{mV}$ high, depending on the op-amp type using the same overvoltage $v_\text{ov} \approx 1.3\,\text{V}$.

Three prototypes have been soldered by the author which make use of the Texas Instruments THS3201 op-amp. One of them has been equipped with a $680\,\Omega$ feedback resistor, the other two use $R_f = 1.2\,\text{k}\Omega$ and $R_f = 2.2\,\text{k}\Omega$, respectively. Figure 4.2 shows the single pulse response of the $680\,\Omega$ and the $1.2\,\text{k}\Omega$ versions. The gain increases by a factor of roughly 1.8 when moving from $680\,\Omega$ to $1.2\,\text{k}\Omega$, so does the maximum of the pulse. This fits nicely to the theory (chapter 2) and prediction. The $2.2\,\text{k}\Omega$ version has been tested, too. Here, the bandwidth has decreased, such that no comparison can be done. Note that the one-stage amplifier design, proposed here, is limited in bandwidth. Only low gain versions can be handeled this way. For
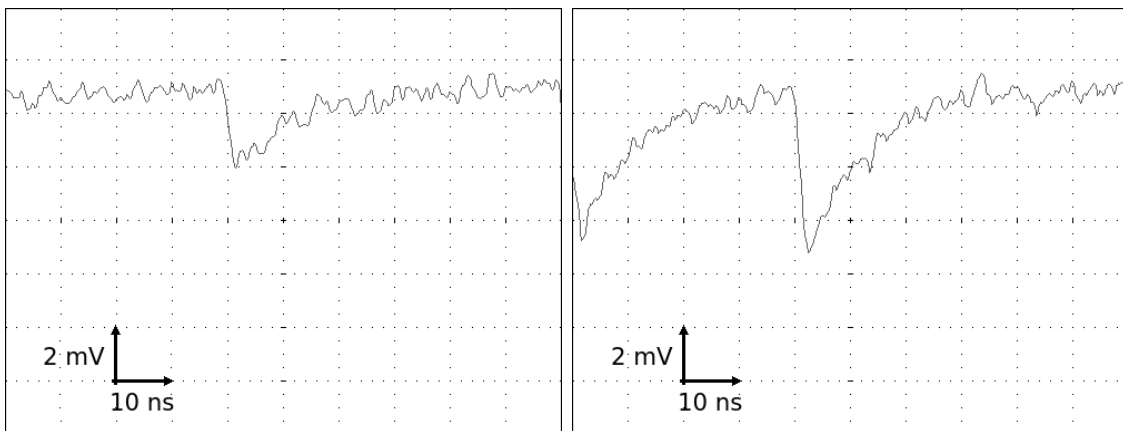
Figure 4.2: Measurement of the SiPM signal output v_o of Texas Instruments THS3201 for two different gain settings using an Hamamatsu S10362-33-050C SiPM. **Left:** $R_f = 680\,\Omega$ and **Right:** $R_f = 1.2\,\text{k}\Omega$.

higher gain, a two-stage amplifier has to be used: For example, a transimpedance amplifier and a non-inverting op-amp in series.

The other op-amps have been equipped with $680\,\Omega$ resistors only. The signal responses of these op-amps are discussed in the next few sections.

4.1.2 Dynamic range

The output voltage of an Intersil EL5165 op-amp at a $50\,\Omega$ load, for example, has been measured to be roughly $-2.9\,\text{mV}$ high for the 1 p.e. peak. The overvoltage at room temperature $T \equiv 25\,°\text{C}$ has been measured to be $v_{\text{ov}} \approx 1.3\,\text{V}$. From the op-amp parameters in table 4.2, the maximal output of the EL5165 is $-1.82\,\text{V}$ at a $50\,\Omega$ load. This corresponds to roughly 630 p.e.

Refering to the datasheet in [37], it is possible to increase the supply voltage of the op-amp to $v_S = 12\,\text{V}$. Using an asymmetric supply $v_{S_+} \to 0^+\,\text{V}$ and $v_{S_-} = -12\,\text{V}$, assuming rail-to-rail[3] support to GND and considering a $50\,\Omega$ load, the maximal number of cells which can be amplified by the op-amp corresponds to about 1500 p.e. Similar calculations apply to Analog Devices AD8014 which is able to read-out 1900 p.e. similtaneously.

From these calculations, you can estimate the optimal value of R_f^{opt} for your design by solving

$$R_f^{\text{opt}} = \frac{v_{\text{sat}}}{N v_o^{1\,\text{p.e.}}(0)} \cdot R_f,$$

where v_{sat} is the negative saturation voltage of the op-amp, N the total number of cells of the SiPM and $v_o^{1\,\text{p.e.}}(0)$ the maximal 1 p.e. output for $t = 0$ of the op-amp

---

[3]An op-amp with "rail-to-rail" support is capable in driving its output from V_{S_-} to V_{S_+}.
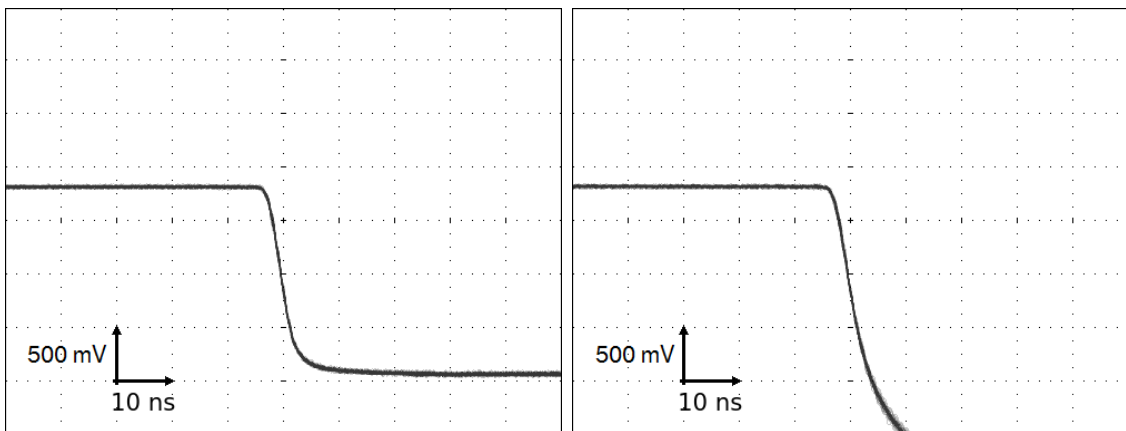
Figure 4.3: Measurement of the large signal response for Texas Instruments THS3201. The op-amp saturated at different levels since the supply voltage has been increased from **left** $\pm 5\,\text{V}$ to **right** $\pm 7.5\,\text{V}$.

with feedback resistance R_f. For the SiPM example above, the AD8014 has to be equipped with $R_f^{\text{opt}} = 360\,\Omega$ to amplify all 3600 cells. Choosing a feedback resistance this low will result in instability, most likely in oscillations.

Figure 4.3 shows the dynamic range measurements that have been done in the laboratory. An SiPM flashed by a bright LED is used as a signal source. The large pulse response of the Texas Instruments THS3201 op-amp has been measured for two different supply voltage $v_{S_\pm}$ configurations. The first one features $v_{S_\pm} = \pm 5\,\text{V}$ and the second one $v_{S_\pm} = \pm 7.5\,\text{V}$. For the smaller supply voltage range, the op-amp has saturated at roughly $-1.7\,\text{V}$. In the other configuration, the op-amp has not saturated at all. If one compares these values with the simulations from above, it is obvious that the op-amp saturates at lower voltages than predicted by the simulation (1.92 V). In the simulation, a perfect setting is assumed: Ideal feedback resistor, ideal voltage source and read-out by an ideal oscilloscope. Also, the simulation is based on a model of an op-amp which might be inaccurate, see discussion in the last and at the beginning of this chapter.

4.1.3 Small signal response

Figure 4.4 shows the small signal response of two selected op-amps to an Hamamatsu S10362-33-050C SiPM measured with the revision B front-end electronics at a $50\,\Omega$ load. This SiPM has 3600 cells and is $3 \times 3\,\text{mm}^2$ in size. The very high bandwidth of the Texas Instruments THS3201 can be seen in this plot. The falling edge is very steep and reaches the maximum of the 1 p.e. in roughly 2 ns. The Maxim MAX4224 is a little bit slower. The fall time is roughly 5 ns. The two values are directly related to the bandwidths of the op-amps, see table 4.1. The response of the slow tail, however, is very similar. This can be linked to the exponential function from theory which is several tens of ns (36 ns from chapter 2 for a typical $3 \times 3\,\text{mm}^2$ Hamamatsu SiPM with 3600 cells) which is well below the bandwidths of the op-amps tested here.

At the beginning of the last chapter, in figure 3.1 on page 27, the small signal response of two other op-amps is shown. The Analog Devices AD8014 and the
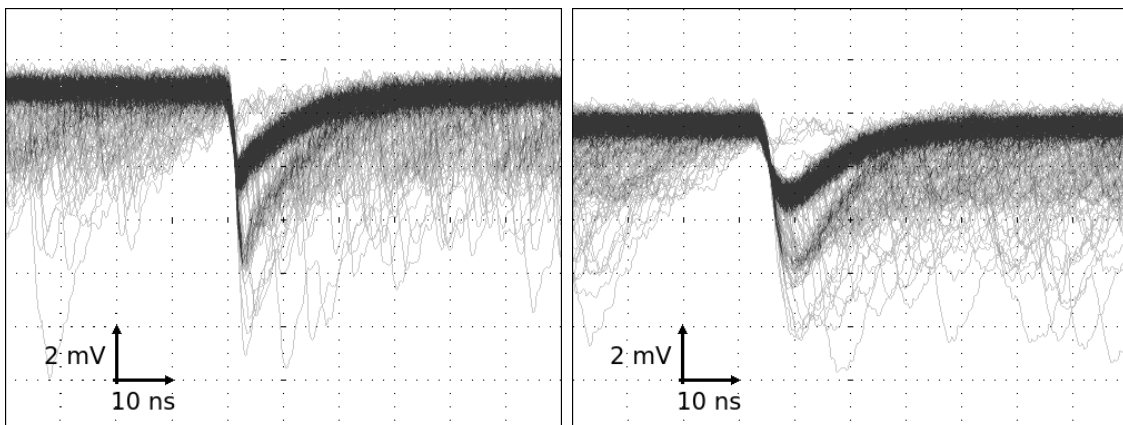
Figure 4.4: Oscilloscope screenshots of the small signal response for two different op-amps. **Left:** Texas Instruments THS3201 and **Right:** Maxim MAX4224.

Intersil EL5165 have smaller simulated bandwidths than both op-amps from above. This is reflected in the response of the falling edge. For the AD8014, the shape of the falling edge matches almost the shape of the slow tail. This means that op-amps with smaller bandwidths than the AD8014 (400 MHz according to [38]) will stretch and smear also the falling edge.

The small pulse response to an Hamamatsu S10362-11-100C SiPM (100 cells and $1 \times 1\,\mathrm{mm}^2$ in size) at a $50\,\Omega$ load has been measured, too. The 1 p.e. maximum is much higher than for the $3 \times 3\,\mathrm{mm}^2$ SiPM from above (about 8 mV compared to 3 mV). This is shown in the appendix in figures A.9 and A.10. This fits nicely to the prediction from theory, see chapter 2. Also, the two components (δ-peak and slow tail) can be imagined.

All op-amps tested in this thesis are fast enough to amplify the slow tail of the SiPM correctly. The steeply falling edge at the beginning of an SiPM pulse is only seen by very fast op-amps, as already mentioned in the last chapter. If timing information is needed, high speed GHz op-amps shall be chosen.
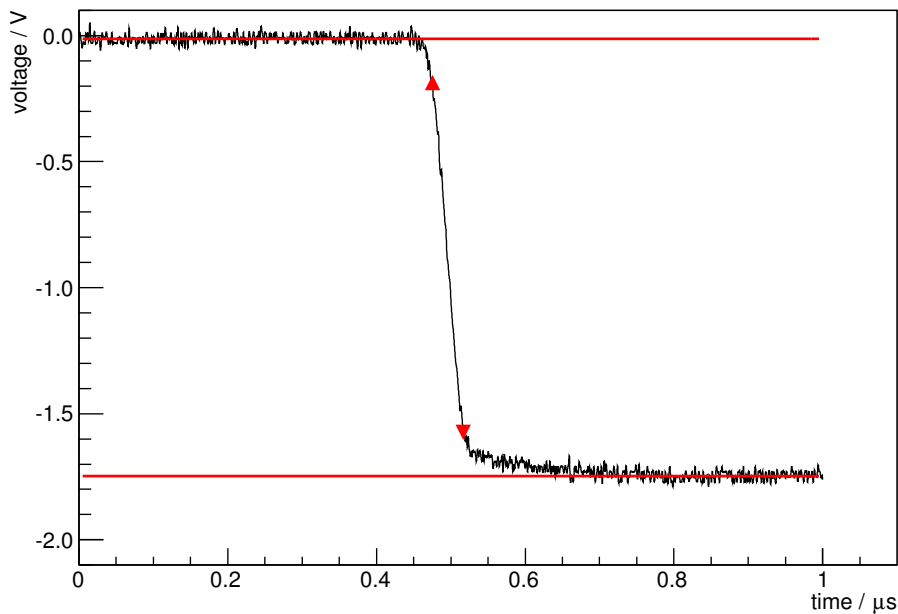
4.1.4   Large signal response

The large signal response can be used to determine the slew rate of an amplifier. A high slew rate is of major importance. For many measurement methods, a gate signal is used. This means that the time interval in which the SiPM signal must lie is limited. Otherwise, the signal fraction inside the gate will decrease linearly with increasing signal height.

The slew rate has been simulated, see table 4.1, and measured, see table 4.2. The simulation parameters have already been introduced. The measurements have been done in the laboratory using the front-end electronics and an SiPM, see figure 4.5. The SiPM has been flashed with an LED. The measurements and simulations cannot be compared directly. This is why the slew rate is denoted with an asterisk in table 4.2. But a qualitative comparison between the various op-amp ICs is possible.

Clearly, the large pulse response of the MAX4224 is smaller than for any of the other tested op-amps. Simulations show that the slew rate of the MAX4224 is roughly 54% of the simulated EL5165 slew rate. Measurements show about 64%. This also fits to the slew rates specified in the datasheets. Also, the slew rates of AD8014, EL5165 and THS3201 are roughly in the same region in the measurement as well as in the simulation.

Some op-amps have higher slew rates than others. This behaviour corresponds to the values given in the simulation table, see above. The slew rate of the Analog Devices AD8014 is of particular interest. It is one of the fastest op-amps for large current pulses, but the slowest for small current pulses of all the op-amps in the test pool. It is seen that the Maxim MAX4224 op-amp is by far the slowest op-amp in the large signal tests. This can be validated by doing comparisons with the specifications in the datasheets given by the manufacturers.

Figure 4.5: Measurement of the large signal response of the Analog Devices AD8014 op-amp to an highly illuminated SiPM. The standard configuration has been used here ($R_f = 680\,\Omega$). The slew rate can be read from the slope of the falling edge, see table 4.2. The red triangles mark 10% and 90% of the pulse height, respectively. Figure A.11 in the appendix shows the same measurement for the Maxim MAX4224 op-amp.
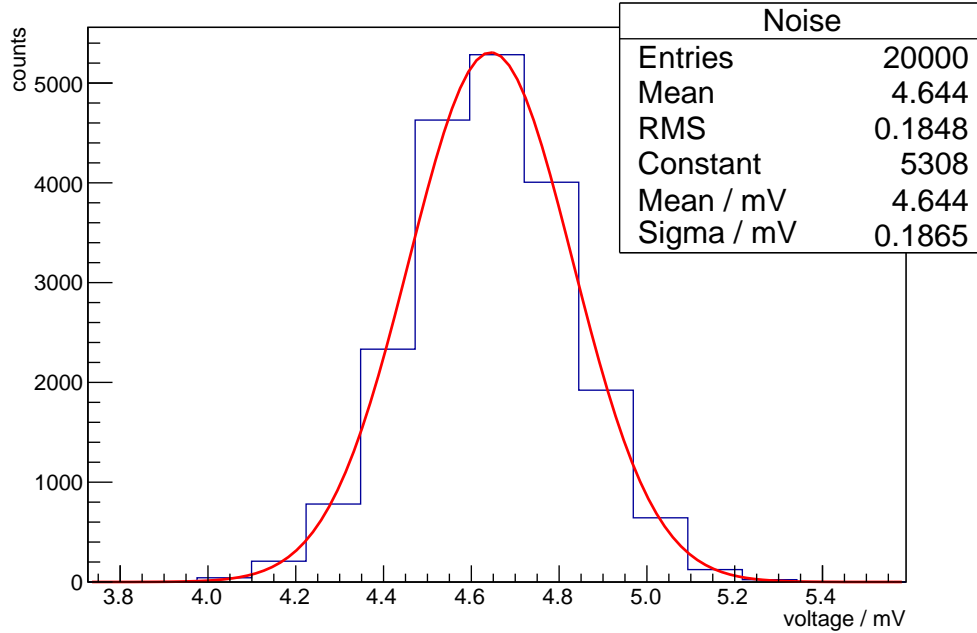
4.1.5 Electronic noise

One way to describe the total noise of a circuit in just one number is by means of the RMS of the noise distribution. Recorded voltage traces of the output of a circuit with an ADC and cables (we call this "equipment" further on) can be presented in a histogram and the RMS can be determined. Since thermal noise and shot noise are purely random signals, the histogram for white noise will follow a Gaussian distribution [41]. Using the standard deviation of this distribution is the easiest way to describe the mean power of the generated white noise. If the pink noise is more dominant, the distributions will not look Gaussian since it decreases in frequency with $1/f$, see section 3.1.4.

However, the recorded data also includes noise effects from the "equipment". To remove this noise one uses a little analytical trick. As shown in an example in the appendix A, the standard deviation σ_h of a Gaussian function h of two convoluted Gaussian distributions $h = (f * g)$ with standard deviations σ_f, σ_g is given by

$$\sigma_h^2 = \sigma_f^2 + \sigma_g^2. \tag{4.1}$$

Since the "equipment" convolutes the noise of the front-end board and its own noise, we let h be the noise distribution of the front-end board measured with the "equip-

Figure 4.6: Histograming $5\,\mu s$ measurement of the electronic noise of the "equipment" and the Texas Instruments THS3201 op-amp h using an oscilloscope. The noise is nearly flat in frequency which results in a Gaussian distributed histogram. The squared standard deviation can be calculated from this plot and subtracted from the other measurements to obtain the noise of the op-amps only, see eq. (4.1).

ment". Then, if we disconnect the board from the "equipment" and take a series of measurements, we will get the noise distribution of the "equipment" itself. We take this to be f. Then, from above, we solve eq. (4.1) for σ_g^2 and finally get the noise distribution for the front-end electronics only.

We use the LeCroy WaveJet 354A which is a $500\,\mathrm{MHz}$ oscilloscope and has an input resistance of $R_i = 50\,\Omega$ per default. This means, that the values measured below are always specified in the bandwidth from $0\,\mathrm{Hz}$ to $500\,\mathrm{MHz}$ and for a $50\,\Omega$ load. From basic voltage divider rules, it is obvious that since the output impedance of the front-end electronics is $R_s = 51\,\Omega$, the output power monitored on the oscilloscope will be roughly one half of the "true" output. Therefore, the final results shown below are given unit-less relative to the one photon equivalent peak $1\,\mathrm{p.e.}$. This cancels out the voltage divider dependence.

Figure 4.6 shows a histogramed $5\,\mu s$ measurement of the "equipment" connected to the front-end board. The board in this figure is equipped with the Texas Instrument THS3201 op-amp and operates without an SiPM h. The distributions are very much Gaussian-like without any systematics. Apparently, the non-Gaussian pink noise can be neglected. To minimise effects from external sources, the measurements have been done several times and the distributions have been checked for each of the measurements. This also gives a certain confidence which describes how well these

Table 4.3: Measurements of the total amplifier noise at $50\,\Omega$ up to $500\,\text{MHz}$ and $V_{s_\pm} = \pm 5\,\text{V}$

Op-amp	Noise / μV	rel. 1 p.e. noise of Ham. S10362-33-050C / %
AD8014	59.68 ± 1.38	2.36 ± 0.19
EL5165	94.13 ± 1.69	3.20 ± 0.23
LMH6703	106.50 ± 2.45	3.39 ± 0.23
MAX4223	67.18 ± 3.16	2.83 ± 0.27
MAX4224	95.58 ± 2.52	3.16 ± 0.23
THS3201	147.03 ± 1.31	4.14 ± 0.24
THS3201 (1k2)	182.29 ± 2.07	2.57 ± 0.12
OPA847 (1k2)	367.86 ± 4.60	-

measurements are reproducible by means of statistical variation. The final results are summarised in table 4.3.

Taking the simulated op-amp parameters into account, see table 4.1, the total integrated noise increases with increasing bandwidth - which is not surprising: If the op-amp or the circuit has a higher bandwidth it can integrate more white noise. The Intersil EL5165 has been chosen for revision F, because it fulfils also the requirements, see chapter 3. Also, the total noise is relatively low which allows low gain measurements. If more gain is needed or if timing for small pulses is essential, an op-amp with higher bandwidth shall be chosen, like the Texas Instruments THS3201.

Obviously, the noise does not increase directly with increasing gain. From table 4.3 we know that increasing the gain by 1.8 ($680\,\Omega \rightarrow 1.2\,\text{k}\Omega$) increases the noise by a factor of 1.2 only . The total noise depends weakly on the gain. To improve the signal to noise ratio, the feedback resistor value R_f has to be increased. A better signal to noise ratio will result in better pulse height separation. For low light level measurements, the gain should be kept as high as possible. If op-amp performance like bandwidth etc. is important either choose a high speed op-amp with high gain or a medium speed op-amp with lower gain.

4.2 Beissel voltage controlling circuit

4.2.1 Temperature compensation

The trimming potentiometer parameter w of the temperature compensation unit has been adjusted to a value, such that the temperature dependence of the breakdown voltage of a Hamamatsu SiPM with $\beta = 56\,\text{mV}\,°\text{C}^{-1}$ can be eliminated. The board has been heated up constantly. During this time, the voltage output of the temperature sensor and the bias voltage have been monitored. The systematic uncertainty of the temperature sensor is taken from the datasheet [40] for the temperature range from $0\,°\text{C}$ to $70\,°\text{C}$. Systematic uncertainties on the measured voltages come from

χ² / ndf	0.7563 / 19
$v_{bd}(0°C)$ / V	69.26 ± 0.03357
β / mVK^{-1}	0.0563 ± 0.001266
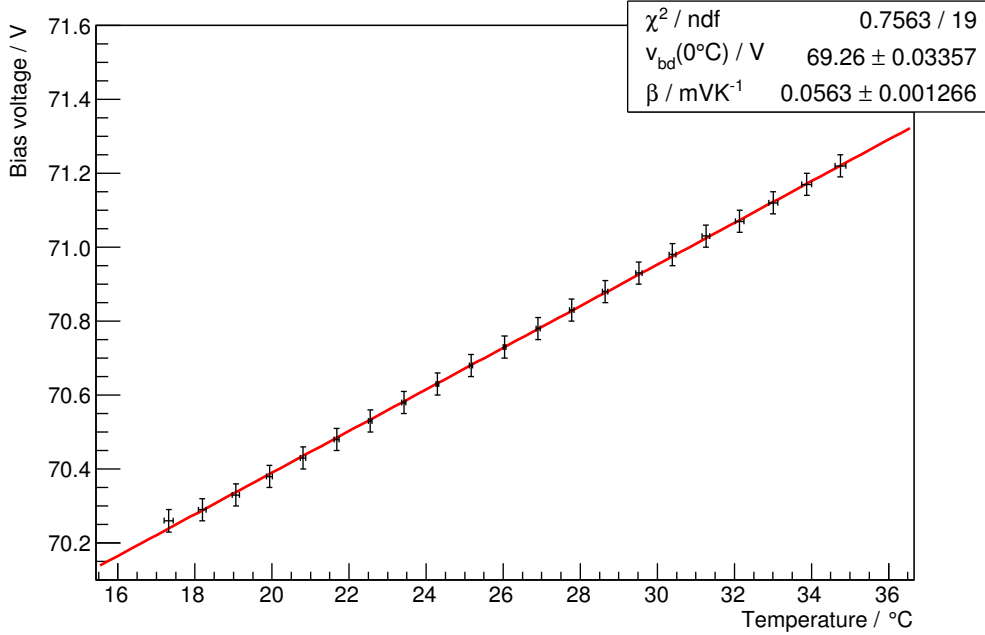
Figure 4.7: Results of the temperature compensation measurement: Bias voltage versus temperature. The errors in this plot are only systematically. Statistical uncertainties are vanishingly small.

Table 4.4: Systematic uncertainties for T compensation (rev.E)

Error source for T	Error	Error source for v_B	Error
AD22100 (typ.) [40]	$-0.014\,T + 0.35\,°C$	v_B resolution	$0.03\,V$
v_T resolution	$0.003\,V \rightarrow 0.13\,°C$		
v_{T+} resolution	$0.003\,V \rightarrow 0.13\,°C$		
Total	(see text)	**Total**	$0.03\,V$

the resolution of the multimeter. Since v_b has been measured with a resolution of $0.1\,V$, it is estimated that the systematic uncertainty is $0.1V/\sqrt{12} \approx 0.03V$. Table 4.4 summarises the systematic uncertainties of this measurement. The temperature has been measured using the onboard temperature sensor output voltage. The resolution of v_T has been $0.01\,V$. This can be converted into a temperature using eq. (3.16) which gives $0.003\,V/\alpha \approx 0.13\,°C$. The same applies to v_{T+}. These uncertainties are added quadratically to get a combined sysematic error [42]. The results of the measurement can be seen in figure 4.7.

The results of the temperature compensation unit look promising. After fitting a polynomial of first degree to the data, redoing the measurement at another day and fitting the linear function again, finally gives

$$\beta_{\text{meas.}} = (56.1 \pm 0.2 \text{ (stat.)} \pm 0.7 \text{ (syst.)}) \text{ mV}\,°C^{-1}. \qquad (4.2)$$
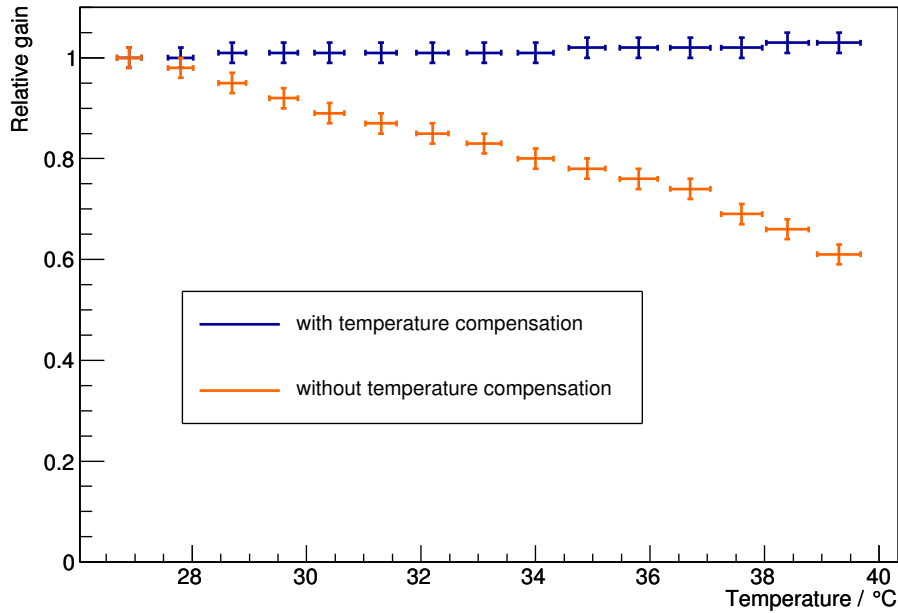
Figure 4.8: Measurement of the SiPM gain relative to $(26.9 \pm 0.2)\,°\mathrm{C}$ versus temperature. In blue, the temperature compensation unit as proposed in this thesis has been activated. The gain is flat over temperature. For a standard read-out, the gain decreases with increasing temperature which is shown in orange.

This measurement can easily be done more accurately by using high sensitive voltmeter devices. Here, standard multimeters have been used. The result fits nicely to the breakdown voltage temperature slope β measured for example in [20] $\beta_{[20]} = (55.7 \pm 0.7)\,\mathrm{mV}\,°\mathrm{C}^{-1}$ and [21] $\beta_{[21]} = (56.6 \pm 0.3)\,\mathrm{mV}\,°\mathrm{C}^{-1}$. The next step is to check, whether the gain of the SiPM will change if the SiPM is heated up, for

- a) the temperature compensation unit turned on

- b) the temperature compensation unit turned off.

This time, the SiPM has been placed into its socket and the LEMO output of the board has been connected to an oscilloscope. A trigger has been set on the 0.5 p.e. falling edge. The gain of the SiPM has then been taken to be the difference between the baseline and the 1 p.e. peak. The board has been heated up and the output voltage of the temperature sensor $v_T(T)$ near the SiPM has been obtained from the monitor port, see last chapter. The temperature has been increasing with approximately constant rate of roughly $0.5\,°\mathrm{C}\,\mathrm{min}^{-1}$.

For the uncompensated measurement, the revision B board with Intersil EL5165 (the same op-amp type like rev.F) has been used. No temperature compensation units are installed here. The same measurements procedures have been done. Since no temperature sensor is installed, the monitor port of the revision F board has

been used once more. The final results of this section are illustrated in figure 4.8. Evidently, the temperature compensation unit also works with an SiPM, i.e. with an active load on the voltage controller which is consuming power.

Over the total measured temperature range from $(26.9 \pm 0.2)\,°C$ to $(39.3 \pm 0.3)\,°C$, the gain of the temperature compensated measurement increases slightly by 2.7%. The uncompensated series of measurement, however, decreases by roughly 36.5%. This can be seen by fitting a polynomial of first degree to the data in figure 4.8. The minimal increase of the compensated version can be eliminated by fine-tuning the potentiometer ratio w.

The approximated linear temperature dependence β can be eliminated with high accuracy since the whole circuit is based on analogue devices only. It depends mostly on how well the trimming potentiometer is being adjusted.

4.3   Conclusion

There is no perfect op-amp in the test bench. All op-amps are very fast; the bandwidths exceed $100\,MHz$ for all of them. Though, most of the op-amps have high noise densities. Depending on the field of use, the following op-amps may be selected:

High light level measurement

For light-intense, i.e. high light flux measurements, a low gain one-stage amplifier must be chosen. Therefore, the input noise density of the op-amp should be low, e.g. by using a low bandwidth op-amp. The Analog Devices AD8014 op-amp with roughly $420\,\Omega$ feedback resistance is sufficient to amplify all 3600 cells of a $3 \times 3\,mm^2$ Hamamatsu SiPM with $50\,\mu m$ cell pitch. This allows full dynamic range measurements.

Low light level measurement

To increase the signal-to-noise ratio, the gain must be increased but the bandwidth suffers from high gain amplifiers. Measurements have shown that the feedback resistance can easily be increased to $1.2\,k\Omega$ without any losses in signal performance. If more gain is needed, a two-stage amplifier will be indispensable. For example, by using a transimpedance amplifier and a non-inverting amplifier in series for negative signal output or an inverting amplifier for positive signal output. Literally, all op-amps can be used for low light level measurements, but the op-amps with medium bandwidth shall be preferred, like Intersil EL5165.

High speed measurement

All op-amps tested in this thesis can be called "high-speed". Thus, high speed measurements can be done with all op-amps. The fastest op-amp for small pulses is Texas Instruments THS3201. This op-amp is inherently fast, even for large pulses.

Temperature compensation

The temperature dependence of the SiPM breakdown voltage has been eliminated successfully. The circuit can be installed very easily and is only based on analogue devices. This circuit can be installed on small physical space and with low costs, see next section.

4.4 Economic aspects

The following calculations are based on small quantity prototypes (≤ 4) of the front-end electronics rev.F board as from October 2013 incl. VAT.

Table 4.5 breaks down the costs for one board including the production of the printed circuit board (PCB) and soldering. The most expensive positions are the PCB and the LEMO connection. The manufacturing process of the PCB has taken one week. The soldering and testing has been done within one working day. Note that the costs for the PCB will be lower if more quantities are ordered from the PCB manufacturer. The same applies to the passive and active components, as well as the terminal connections.

Table 4.5: Costs per board (rev.F) as from October 2013 incl. VAT

Position	Price / €
Printed circuit board	24.62
Passive components (Resistors, Capacitors, ...)	2.67
Active components (ICs)	6.22
Terminals (Box header, LEMO connection, ...)	14.12
Total	47.24

5. Summary and Outlook

In his thesis, the author has developed fully analogue working front-end electronics for the characterisation of silicon photomultipliers (SiPMs). These front-end boards make successfully use of GHz operational amplifiers (op-amps) for the amplification of SiPM signals. Also, these boards are designed in pure transimpedance mode. The front-end electronics includes a temperature compensation unit which can eliminate the temperature dependence of the breakdown voltage $v_{\mathrm{bd}}(T)$ for a wide range of SiPMs. The boards do not suffer from disadvantages of standard read-out circuits, like the voltage drop at the SiPM current limiting resistor for small currents.

This is a selection of the advantages of the front-end electronics introduced in this thesis. The boards have been successfully used for amplification of the SiPM signal. Even SiPM characterisation studies have been performed.

At the beginning of this thesis (chapter 2), the equivalent circuit of an SiPM model has been introduced. The responses of passive and active current-to-voltage converters have been calculated analytically and the active version using a transimpedance amplifier has been chosen. Non-ideal op-amp parameters have been presented (chapter 3) and measured in the laboratory (chapter 4). Here, the features mentioned at the beginning of this summary have been quantified for various op-amps. The temperature compensation unit has been used to eliminate the temperature dependence of the SiPM breakdown voltage which is directly related to the SiPM gain.

However, the front-end electronics are not limited to characterisation studies only. Also, experiments in high-energy physics or astro-particle physics can be equipped with these preamplifiers. Further possible options are the usage in practical lessons on physics, physical training period or physics pratical course. Since only analogue devices have been used in the electronics, the amplifier boards are low-priced and small.

In the near future, these boards are used to do characterisation studies of SiPMs. Several manufacturers have released new types of SiPMs with lower correlated noise rates and higher photon detection efficiencies. These SiPMs will be characterised for the installation in the FAMOUS telescope, a fluorescence detector prototype which is the first of its kind making use of SiPMs.

A bright future in photo-detection lies ahead.

A. Appendix

Integral transforms

Laplace transform

The Laplace[1] transform $F(s)$ of a function $f(t)$, with $t \geq 0$ and $s \in \mathbb{C}$ is defined by

$$F(s) = \mathcal{L}\left\{f(t)\,;\, t\,;\, s\right\}$$
$$\equiv \int\limits_{0^-}^{\infty} dt\, f(t)\, e^{-st}. \tag{A.1}$$

Since $s = \Re(s) + j\,\Im(s)$ is a complex number, the inverse Laplace transform is then given by

$$f(t) = \mathcal{L}^{-1}\left\{F(s)\,;\, s\,;\, t\right\}$$
$$\equiv \frac{1}{2\,\pi\,j} \lim_{T \to \infty} \int\limits_{\gamma - j\,T}^{\gamma + j\,T} ds\, F(s)\, e^{s\,t}, \tag{A.2}$$

---

[1]Named after Pierre-Simon, marquis de Laplace (1749 - 1827), French mathematician and astronomer

Table A.1: Laplace transform pairs, taken from [43]

$\mathbf{f(t)}$	$\mathbf{F(s)}$
$f(t - t')$	$F(s)\, e^{-st'}$
$\frac{d}{dt} f(t)$	$s\, F(s) - f(t \to 0^-)$
$\delta(t)$	1
$u(t)$	s^{-1}
$f(0)\left(c\, e^{-t/\tau_+} + (1 - c)\, e^{-t/\tau_-}\right)$	$\frac{1 + a_0 s}{a_1 + a_2 s + a_3 s^2}$

Variable	Substitution
$f(0)$	$\frac{a_0}{a_3}$
c	$\frac{1}{2} + \frac{a_2/2 - a_3/a_0}{\sqrt{a_2^2 - 4a_1 a_3}}$
$\tau_\pm$	$\frac{2a_3}{a_2 \pm \sqrt{a_2^2 - 4a_1 a_3}}$

where $\gamma \in \mathbb{R}$ is chosen such that the integral contour path becomes convergent. The Laplace transform transfers a linear differential equation to an analytical equation, which is usually much easier to solve; The transform of a derivative of a function in the t-domain $d/dt\, f(t)$ is linear to s in the s-domain, see table A.1.

Examples

Applying a voltage $v_C(t)$ across a capacitor with capacitance C creates a charge separation

$$q_C(t) = C\, v_C(t).$$

The current $i_C(t)$ through the capacitor is then defined as

$$i_C(t) \equiv \frac{d}{dt} q_C(t)$$
$$= C\, \frac{d}{dt} v_C(t)$$

assuming $C = $ const.. Using the Laplace transform of the derivation from table A.1 finally gives

$$I_C(s) = sC\, V_C(s) - C\, v_C(t \to 0^-), \qquad (A.3)$$

which can be diagrammed graphically, see figure A.1. Similar calculations apply to an inductor L

$$v_L(t) = L\frac{d}{dt}\, i_L(t)$$
$$\Leftrightarrow V_L(s) = sLI_L(s) - Li_L(t \to 0^-)$$
$$\Leftrightarrow I_L(s) = \frac{V_L(s)}{sL} + \frac{i_L(t \to 0^-)}{s}, \qquad (A.4)$$

figure A.1. The equations of a resistor R are the same in both Laplace domains

$$v_R(t) = Ri_R(t)$$
$$\Leftrightarrow V_R(s) = RI_R(s). \qquad (A.5)$$
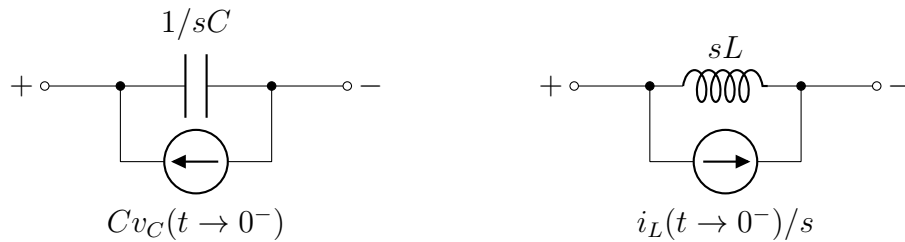
Figure A.1: Left: An s-domain circuit of a capacitor with capactiance C and t-domain voltage drop v_C for $t \to 0^-$, used for calculations of the SiPM model in chapter 2 and 3. The impedance of the capacitor becomes $Z_C(s) = 1/sC$. **Right:** An s-domain circuit of an inductor with inductance L and t-domain current i_L for $t \to 0^-$, used for calculations of the low pass filter in chapter 4.

Fourier transform

The one-dimensional Fourier[2] transform $\hat{f}(k)$ of a function $f(x)$, with k, $x \in \mathbb{R}$, is defined by

$$
\begin{aligned}
\hat{f}(k) &= \mathcal{F}\left\{f(x)\,;\,x\,;\,k\right\} \\
&\equiv \frac{1}{\sqrt{2\,\pi}} \int\limits_{-\infty}^{\infty} dx\, f(x)\, e^{-j\,k\,x}.
\end{aligned}
\tag{A.6}
$$

The inverse Fourier transform is simply

$$
\begin{aligned}
f(x) &= \mathcal{F}^{-1}\left\{\hat{f}(k)\,;\,k\,;\,x\right\} \\
&\equiv \mathcal{F}\left\{\hat{f}(k)\,;\,k\,;\,x\right\}.
\end{aligned}
\tag{A.7}
$$

Table A.2: Fourier transform pairs, taken from [43] and [44]

$\mathbf{h(x)}$	$\mathbf{\hat{h}(k)}$
$(f * g)(x)$	$\hat{f}(k) \cdot \hat{g}(k)$
$(2\,\pi\,\sigma^2)^{-1/2}\,\exp\left(-(x-\mu)^2/\,2\,\sigma^2\right)$	$\exp\left(\sigma^2\,k^2/\,2 - j\,\mu\,k\right)$

Examples

Let $f(x)$ and $g(x)$ be normal distributed functions and $h(x) = (f * g)(x)$, then, with table A.2,

$$
\begin{aligned}
\hat{h}(k) &= \hat{f}(k) \cdot \hat{g}(k) \\
&= \exp\left(\sigma_f^2\,k^2/\,2 - j\,\mu_f\,k\right) \cdot \exp\left(\sigma_g^2\,k^2/\,2 - j\,\mu_g\,k\right) \\
&= \exp\left(\left(\sigma_f^2 + \sigma_g^2\right)\,k^2/\,2 - j\,(\mu_f + \mu_g)\,k\right).
\end{aligned}
$$

Applying the inverse Fourier transform immediately solves to

$$
h(x) = \left(2\,\pi\,\sigma_h^2\right)^{-1/2}\,\exp\left(-(x-\mu_h)^2/\,2\,\sigma_h^2\right)
$$

$$
\begin{aligned}
\sigma_h^2 &= \sigma_f^2 + \sigma_g^2 \\
\mu_h &= \mu_f + \mu_g,
\end{aligned}
$$

such, that $h(x)$ becomes normal distributed, too. $\sigma_{f,g,h}$ and $\mu_{f,g,h}$ are standard deviation and mean of the normal distributions $f(x)$, $g(x)$ and $h(x)$, respectively.

---

[2]Named after Jean Baptiste Joseph Fourier (1768 - 1830), French mathematician

Electronical parameters of Silicon Photomultipliers

SiPM type	Size / mm^2	N	R_q / kΩ	C_q / fF	C_d / fF	C_g / pF
Hamamatsu S10362-11-100C	1×1	100	118.1 ± 0.3	71.8 ± 12.5	318.0 ± 0.5	6.8 ± 1.0
Hamamatsu S10362-33-050C	3×3	3600	151.2 ± 0.4	100.1 ± 9.0	83.3 ± 1.0	9.3 ± 1.7

Table A.3: Parameters of the SiPM model, taken from [31]

Deriving the avalanche charge Q generated in a breakdown of M SiPM cells

In 1996, Cova et al published an equivalent circuit of an avalanche photodiode [45]. The basic schematic of this paper will be adopted in the following derivation of the charge which is generated in a breakdown of a cell of an SiPM. Calculations have been performed by the author of this master thesis.
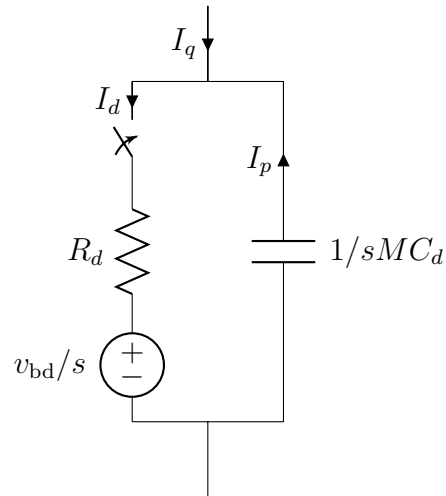
Figure A.2: Circuit for the motivation of the current pulse in the SiPM model in figure 2.4, see equation (2.3). For the derivation in this chapter, the diode, i.e. current source and diode capacitance, have to be replaced in the model of chapter 2 with this circuit.

The SiPM model introduced in chapter 2 will be used, see figure 2.4. Instead of the current source and diode capacitance in the firing cell, the equivalent circuit from figure A.2 is implemented. The switch is closed at time $t = 0$ and opened shortly after $\mathcal{O}(\text{ps})$. This is the duration of the breakdown. A transimpedance amplifier is used for reading-out the SiPM, like pictured in figure 2.6. The currents and current relations from chapter 2.3.2.2 apply also to this circuit, except for

$$I_d = \frac{V' - v_{\text{bd}}/s}{R_d}. \tag{A.8}$$

Using equations 2.15 and 2.19 and solving for V' gives

$$V'(s) = \frac{Mv_b R_d R_q (C_q + C_d)s + Mv_b R_d + v_{\text{bd}} R_q}{MR_d R_q (C_q + C_d)s^2 + MR_d + R_q}. \tag{A.9}$$

Remember that we have not re-opened the switch yet. Plugging eq. A.9 into A.8 gives

$$I_d(s) = Mv_{\text{ov}} \frac{R_q(C_q + C_d)s + 1}{MR_d R_q (C_q + C_d)s^2 + (MR_d + R_q)s}, \tag{A.10}$$

where $v_{\text{ov}} \equiv v_b - v_{\text{bd}}$ has been used. The diode resistance R_d is vanishingly small compared to the quenching resistance R_q, i.e. $R_d \ll R_q$. Transforming the equation into a taylor series expansion and ignoring any orders of R_d/R_q results in

$$
\begin{aligned}
I_d(s) &\approx M v_{\text{ov}} \left(\frac{1}{sR_q} + C_q + C_d \right) \\
\Leftrightarrow i_d(t) &\approx M v_{\text{ov}} \left(\frac{1}{R_q} + (C_q + C_d)\delta(t) \right).
\end{aligned}
\tag{A.11}
$$

The first summand $M v_{\text{ov}}/R_q$ is a t-domain constant current and very small compared to the latter. We also claimed that the pulse must be really short in time and we have not re-opened the switch yet. When we ignore the first term, we finally obtain the charge as proposed in chapter 2

$$
i_d(t) \approx M v_{\text{ov}}(C_q + C_d)\delta(t). \tag{A.12}
$$

This current pulse is only an approximation. For example, if also the linear order of the taylor expansion from equation A.10 is used, the resulting charge will be smaller than A.11 because the linear order is negative. Therefore, one can say that the charge derived here is an upper limit of the typical SiPM charge created in an avalanche process.

Instead of choosing the δ function only, it is possible to use the integral of the not-expanded t-domain solution of $i_d(t)$ for example from $t = 0\tau$ to $t = 5\tau$, where τ is the time constant of the not-expanded function $i_d(t)$. This charge can be multiplied with a δ function and used for calculations, too. This method actually yields nearly the same result as the prior variant.

Front-end electronics layout
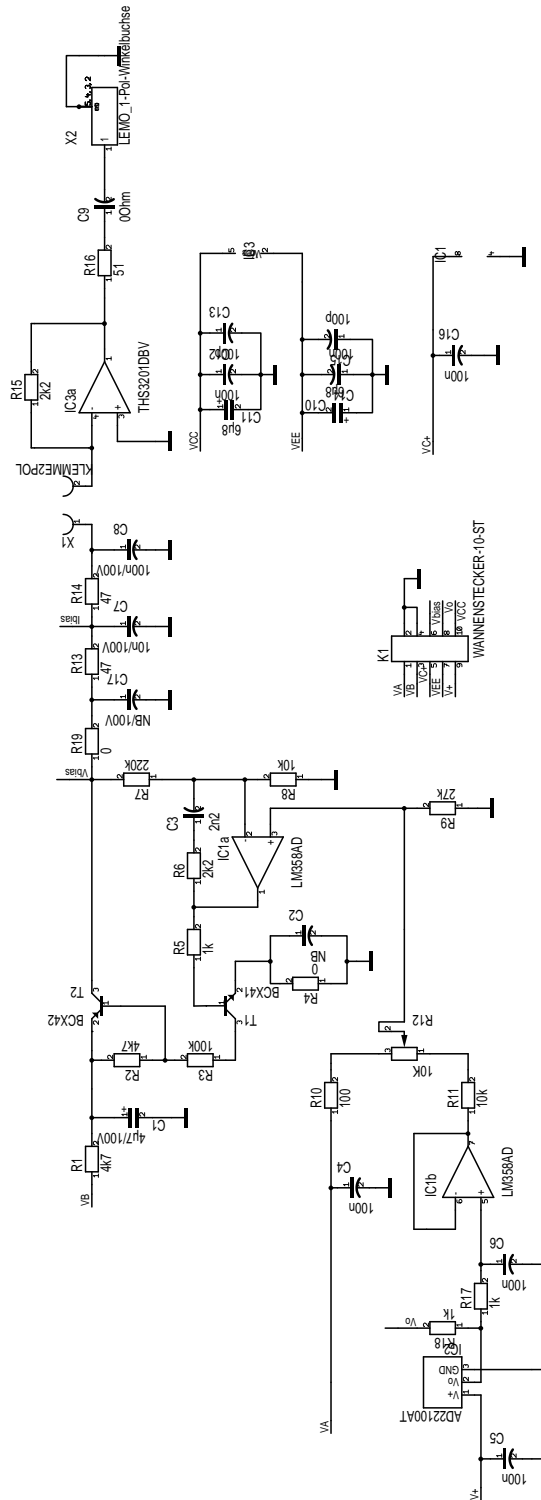
Figure A.3: Full read-out layout proposed in this thesis: Transimpedance amplifier, passive LC low-pass filter, current limitation and temperature compensation are described in detail in chapter 2 and chapter 3.

Exact solutions of temperature compensation unit

$$w(\beta) = \frac{1}{2} - \frac{R_1 - R_2}{2R_p} + \frac{R_g}{2R_p}\frac{\alpha}{\beta}\left(\left(1 + \frac{R_6}{R_7}\right) - \sqrt{\left(\left(1 + \frac{R_6}{R_7}\right) - \frac{R_1 + R_2 + R_p\frac{\beta}{\alpha}}{R_g}\right)^2 + 4\frac{R_1 + R_2 + R_p}{R_g}\left(\frac{\beta}{\alpha}\right)^2}\right) \tag{A.13}$$

$$v_a(w) = \left(1 + \frac{R_2 + (1-w)R_p}{R_1 + wR_p} + \frac{R_2 + (1-w)R_p}{R_g}\right)\frac{v_{\mathrm{bd}}(0\,°\mathrm{C}) + v_{\mathrm{ov}}}{1 + R_6/R_7} - \frac{R_2 + (1-w)R_p}{R_1 + wR_p}v_T(0\,°\mathrm{C}) \tag{A.14}$$

Datasheet of the front-end electronics rev.F developed by J. Schumacher
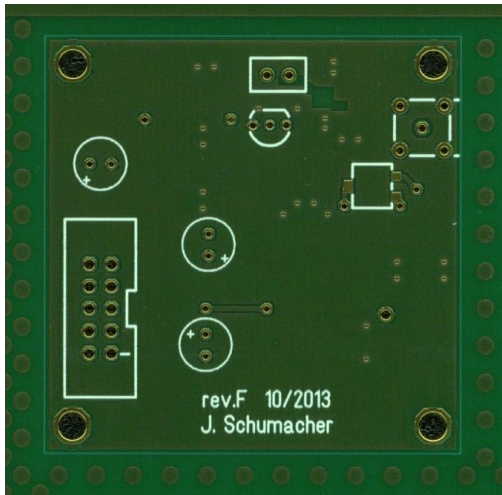
Figure A.4: Top view
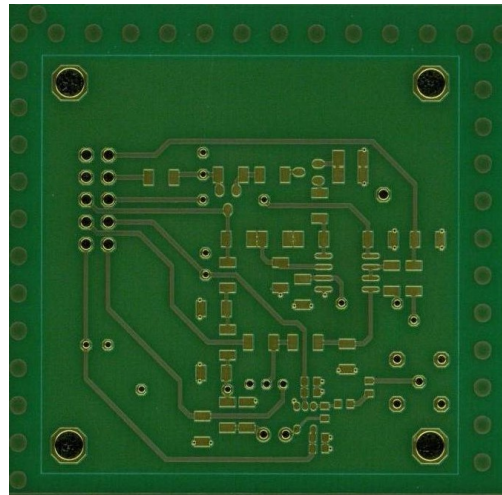
Figure A.5: Bottom view

Features

- High-speed transimpedance amplifier op-amp in SOT23/5 package

  - High bandwidth (GHz)
  - High slew rate ($kV\mu s^{-1}$)

- Low integrated noise (3% of a $3 \times 3\,mm^2$, 3600 cells Hamamatsu SiPM 1 p.e. peak)

- Temperature compensation of SiPM breakdown voltage ($\beta = 10\ldots80\,mV\,°C^{-1}$)

- bias voltages v_b of up to 100 V (125 V possible)

The front-end electronics rev.F is a fully anlaogue working preamplifier for silicon photomultipliers (SiPMs). It offers features for filtering of the bias voltage v_b, current limitation of the SiPM, active current-to-voltage conversion of the SiPM signal via high speed transimpedance amplifier (GHz bandwidth and several $1000\,V\mu s^{-1}$ slew rate) and

correction of the temperature dependence of the SiPM breakdown voltage $v_{bd}(T)$. It supports SiPM temperature slopes of $\beta = 10\ldots80\,mV\,°C^{-1}$ in the standard configuration (from the minimum to the maximum value of the trim pot). This range can be extended easily by changing resistor values in the analogue Beissel Voltage Controlling (BVC) circuit and temperature compensation unit developed in this thesis. The slope is adjusted by trimming the potentiometer on the top side of the amplifier board. The bias voltage can be varied by changing the adjust voltage v_a depending on the value of the potentiometer.

Table A.4: Adjust voltage v_a and resulting bias voltage v_b at $T \equiv 25\,°C$ and $\beta = 56\,mV°C^{-1}$

v_a / V	v_b / V	v_a / V	v_b / V
3.30	69.24	3.40	71.20
3.32	69.63	3.42	71.59
3.34	70.03	3.44	71.98
3.36	70.41	3.46	72.37
3.38	70.81	3.48	72.76

The *box header* which is connected at the top side of the front-end board, see photo, supplies the integrated circuits (ICs) and SiPM. Pins 2, 4, 5, 7, 9 and 10 are reserved for supply voltages of the ICs. The temperature sensor output is sensitive to the supply voltage. v_+ must be set to $+5\,\mathrm{V}$ very accurately. Pin 6 and 8 are monitor pins only. There must not be applied any voltage at these nodes! The bias voltage can be monitored at pin 6. The temperature can be read-out at pin 8 and interpreted by using the formula

$$T/^\circ\mathrm{C} = \frac{v_T - 1.375\,\mathrm{V}}{22.5\,\mathrm{mV}}$$

in the default configuration.
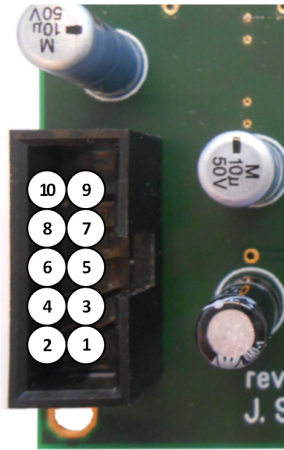
Figure A.6: Box header

Pin	Node	Typ.
1	v_a	$+3.3\,\mathrm{V}$
2	GND	GND
3	v_i	$+80\,\mathrm{V}$
4	GND	GND
5	v_{C_+}	$+5\,\mathrm{V}$
6	v_{bias}	(mon.)
7	v_{S_-}	$-5\,\mathrm{V}$
8	v_T	(mon.)
9	v_+	$+5\,\mathrm{V}$
10	v_{S_+}	$+5\,\mathrm{V}$

The front-end electronics is usually shipped with the default values introduced in this thesis. Some parameters like the RC and LC filter and some resistors in the BVC may be changed without any loss in performance. The important parameters and their default values are printed in the table. If you make any changes, there will be enough space to write down the new settings. The element names (R_7, R_8, ...) can be obtained from the TARGET 3001! circuit diagram attached in the master thesis.

| Element	Default	Note
Op-amp	EL5165	
R_f	$680\,\Omega$	
R_7	$220\,\mathrm{k\Omega}$	
R_8	$10\,\mathrm{k\Omega}$	
R_p	$2\,\mathrm{k\Omega}$	
R_9	$27\,\mathrm{k\Omega}$	
R_{10}	$100\,\Omega$	
R_{11}	$10\,\mathrm{k\Omega}$	
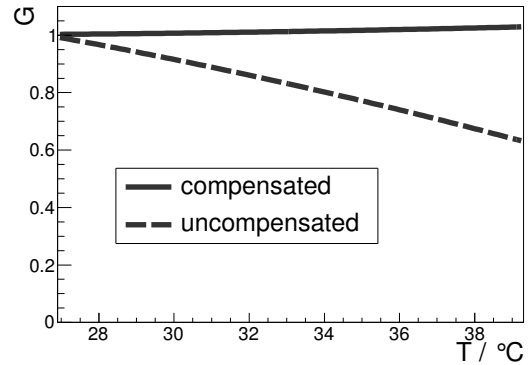
Figure A.7: Gain stability over T
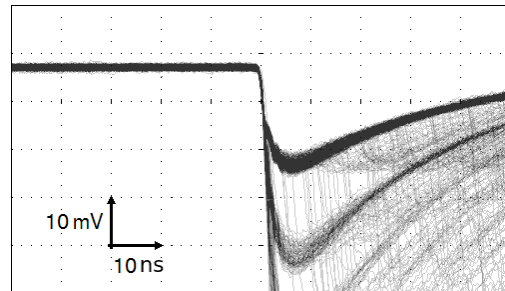
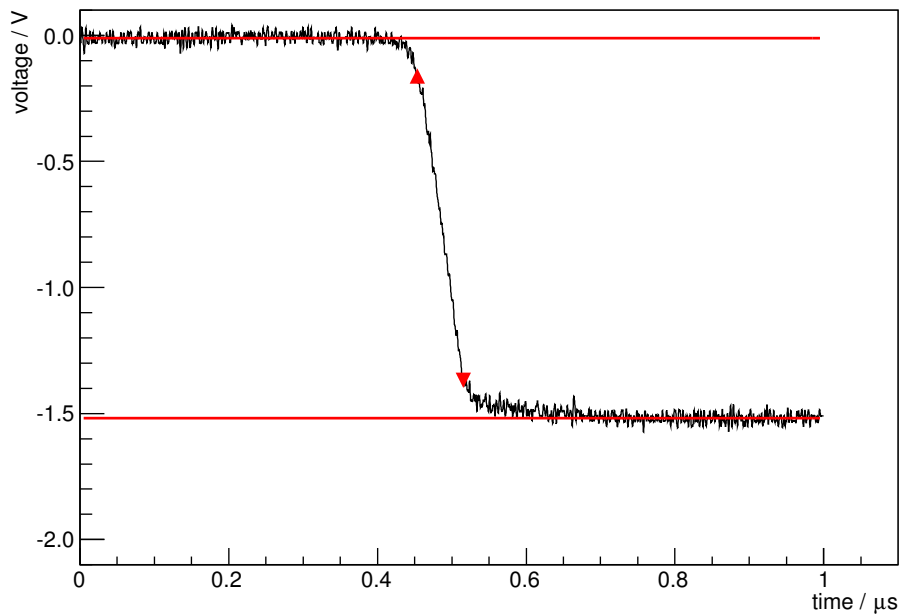
Figure A.8: THS3201, $R_f = 2.2\,\mathrm{k\Omega}$

Additional graphics
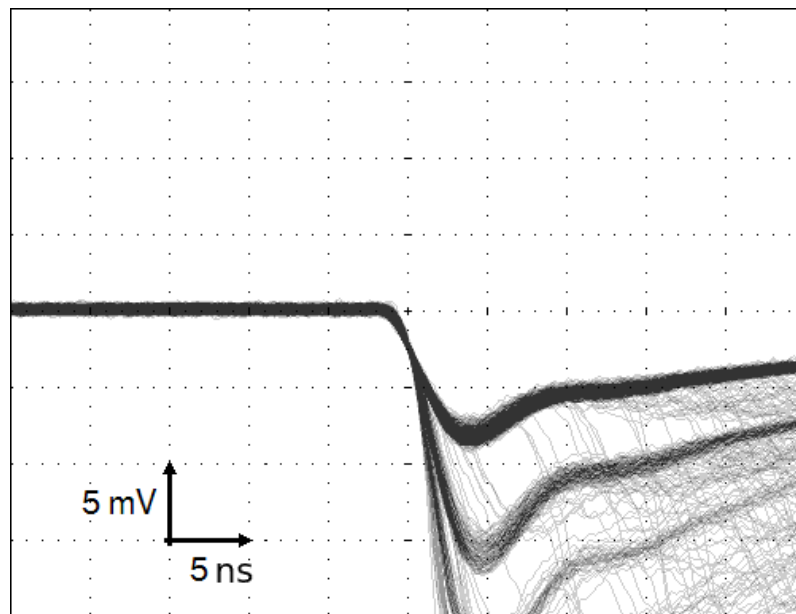
Figure A.9: Oscilloscope screenshot of a Hamamatsu S10362-11-100C SiPM signal amplified with the front-end electronics (rev.B) developed in this thesis using an Analog Devices AD8014 op-amp. Compare with figure A.9.
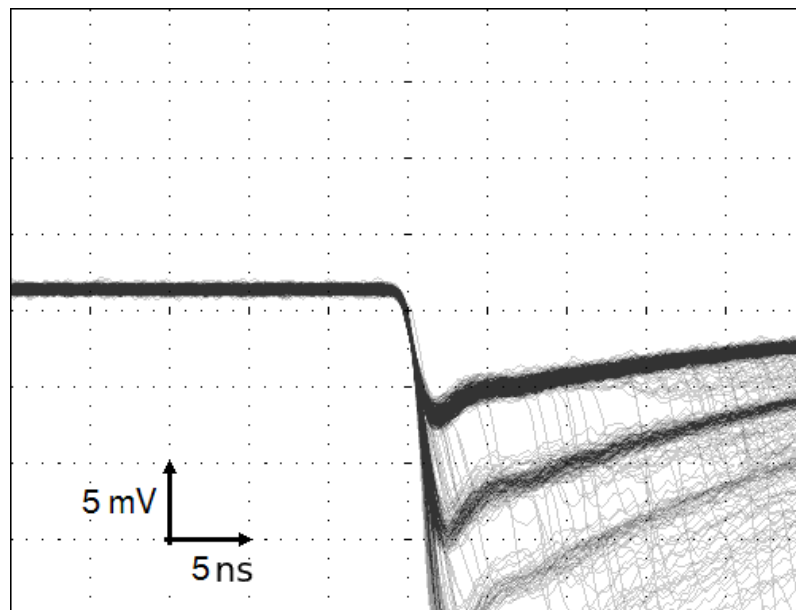
Figure A.10: Like figure A.10 using an Intersil EL5165 op-amp.

Figure A.11: Measurement of the large signal response of the Maxim MAX4224 op-amp to an highly illuminated SiPM. The standard configuration has been used here ($R_f = 680\,\Omega$). The slew rate can be read from the slope of the falling edge, see table 4.2. The red triangles mark 10% and 90% of the pulse height, respectively.
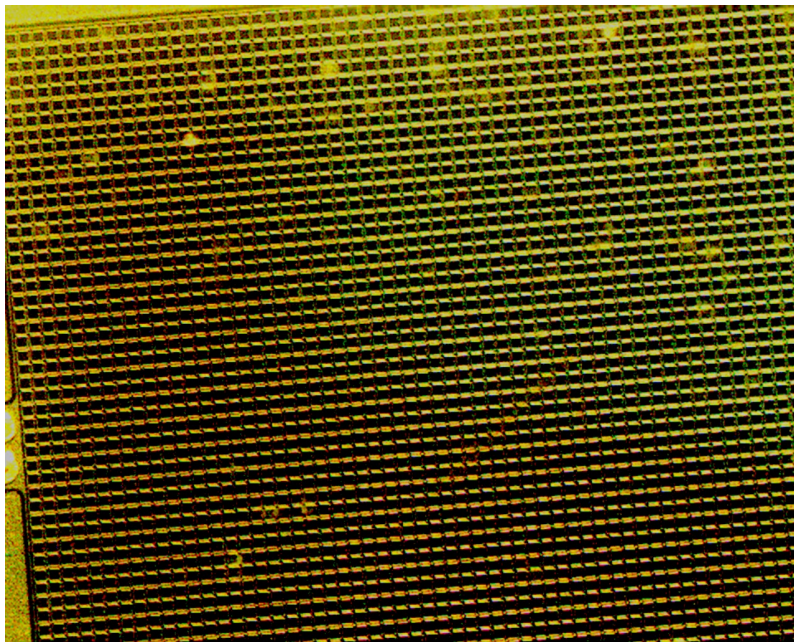
Figure A.12: False colour microscope image of an Hamamatsu S10362-33-050C silicon photomultiplier (SiPM) taken by the author. Each G-APD cell (black squares) is $50 \times 50\,\mu\text{m}^2$. The blurred spots come from dirt and defects in the epoxy resin on the surface of the SiPM.

References

[1] V. F. HESS, *Über Beobachtungen der durchdringenden Strahlung bei sieben Freiballonfahrten*, Z. Phys., 13 (1912), p. 1084.

[2] J. BERINGER et al., *Review of Particle Physics 2012*, Phys. Rev. D, 86 (2012), p. 010001.

[3] T. P. A. COLLABORATION, *The Pierre Auger Observatory: Contributions to the 33rd International Cosmic Ray Conference (ICRC 2013)*, (2013).

[4] T. K. GAISSER, *Cosmic Rays and Particle Physics*, Cambridge University Press, Cambridge, 1 ed., 1990.

[5] K. GREISEN, *End to the Cosmic-Ray Spectrum?*, Phys. Rev. Lett., 16 (1966), pp. 748–750.

[6] G. T. ZATSEPIN AND V. A. KUZ'MIN, *Upper Limit of the Spectrum of Cosmic Rays*, JETP Letters, 4 (1966), pp. 78–80.

[7] T. GAISSER AND A. M. HILLAS, *Reliability of the method of constant intensity cuts for reconstructing the average development of vertical showers*, Proceedings of the 15th ICRC, 8 (1977), p. 353.

[8] T. P. A. COLLABORATION, *The Fluorescence Detector of the Pierre Auger Observatory*, (2009).

[9] D. ZAVRTANIK, *The Pierre Auger Observatory*, Nuclear Physics B - Proceedings Supplements, 85 (2000), pp. 324 – 331.

[10] I. ALLEKOTTE et al., *The surface detector system of the Pierre Auger Observatory*, Nuclear Instruments and Methods in Physics Research Section A: Accelerators, Spectrometers, Detectors and Associated Equipment, 586 (2008), pp. 409 – 420.

[11] T. DANDL, T. HEINDL, AND A. ULRICH, *Fluorescence of nitrogen and air*, Journal of Instrumentation, 7 (2012), p. P11005.

[12] C. MEURER AND N. SCHARF ON BEHALF OF THE PIERRE AUGER COLLABORATION, *HEAT - a low energy enhancement of the Pierre Auger Observatory*, (2011).

[13] P. ABREU et al., *The Pierre Auger Observatory V: Enhancements*, arXiv preprint arXiv:1107.4807, (2011).

[14] P. Abreu *et al.*, *Antennas for the detection of radio emission pulses from cosmic-ray induced air showers at the Pierre Auger Observatory*, Journal of Instrumentation, 7 (2012), p. P10011.

[15] H. Klages and the Pierre Auger Collaboration, *Enhancements to the Southern Pierre Auger Observatory*, Journal of Physics: Conference Series, 375 (2012), p. 052006.

[16] M. Stephan *et al.*, *Future use of silicon photomultipliers for the fluorescence detection of ultra-high-energy cosmic rays*, 2011.

[17] *Obituaries - Boris Dolgoshein*. http://cerncourier.com/cws/article/cern/45162, Feb 23, 2011.

[18] G. Bondarenko *et al.*, *Limited Geiger-mode microcell silicon photodiode: new results*, Nuclear Instruments and Methods in Physics Research Section A: Accelerators, Spectrometers, Detectors and Associated Equipment, 442 (2000), pp. 187 – 192.

[19] D. Renker, Paul Scherrer Institute, Villigen, Switzerland, *Advances in solid state photon detection*, Journal of Instrumentation, 4 (2009).

[20] J. Schumacher, *Characterization Studies of Silicon Photomultipliers: Noise and Relative Photon Detection Efficiency*, bachelor thesis, III. Phys. Inst. A, RWTH Aachen University, Germany, February 2011.

[21] M. Lauscher, *Characterisation Studies of Silicon Photomultipliers for the Detection of Fluorescence Light from Extensive Air Showers*, master thesis, III. Phys. Inst. A, RWTH Aachen University, Germany, January 2012.

[22] Hamamatsu, *S10362-33-050C datasheet, visited on 29 November 2013*. https://www.hamamatsu.com/resources/pdf/ssd/s10362-33_series_kapd1023e05.pdf, 2009.

[23] Excelitas, *C30742-33 datasheet, visited on 29 November 2013*. http://www.excelitas.com/downloads/DTS_C30742-33_Series_SiPM.pdf, 2013.

[24] Hamamatsu, *Private communication*, 2013.

[25] Excelitas, *Private communication*, 2013.

[26] Ketek, *PM3350 datasheet, visited on 29 November 2013*. http://www.ketek.net/products/sipm/pm3350, 2012.

[27] Ketek, *SiPM world record for photon detection efficiency, visited on 29 November 2013*. http://www.ketek.net/news/product-and-company-news/news-details/?tx_ttnews[year]=2013&tx_ttnews[month]=04&tx_ttnews[day]=26&tx_ttnews[tt_news]=54&cHash=f88abc7fd039deafde8e82030e6f0cd3, 2013.

[28] J. Bird, *Electrical Circuit Theory and Technology*, Newnes, 2 ed., 2010.

[29] F. Corsi *et al.*, *Electrical Characterization of Silicon Photo-Multiplier Detectors for Optimal Front-End Design*, in Nuclear Science Symposium Conference Record, 2006. IEEE, vol. 2, 2006, pp. 1276–1280.

[30] F. Corsi *et al.*, *Modelling a silicon photomultiplier (SiPM) as a signal source for optimum front-end design*, Nuclear Instruments and Methods in Physics Research Section A: Accelerators, Spectrometers, Detectors and Associated Equipment, 572 (2007), pp. 416 – 418.

[31] F. Scheuch, *Measurement and simulation of electrical properties of SiPM photon detectors*, master thesis, III. Phys. Inst. A, RWTH Aachen University, Germany, November 2012.

[32] Linear Technology Corporation, *LTspice IV website, visited on 1 December 2013.* http://www.linear.com/ltspice.

[33] Ing.-Büro Friedrich, *TARGET3001! website, visited on 1 December 2013.* http://www.ibfriedrich.com.

[34] Texas Instruments, *THS3201 datasheet.* http://www.ti.com/lit/ds/slos416c/slos416c.pdf, 2009.

[35] Maxim Integrated, *MAX4224 datasheet.* http://datasheets.maximintegrated.com/en/ds/MAX4223-MAX4228.pdf, 1997.

[36] Ron Mancini - Texas Instruments, *Op Amps For Everyone - Design Reference.* http://www.ti.com/lit/an/slod006b/slod006b.pdf, August 2002.

[37] Intersil, *EL5165 datasheet.* http://www.intersil.com/content/dam/Intersil/documents/fn73/fn7389.pdf, 2007.

[38] Analog Devices, *AD8014 datasheet.* http://www.analog.com/static/imported-files/data_sheets/AD8014.pdf, 2010.

[39] H. T. Friis, *Noise figures of radio receivers*, Proceedings of the IRE, 32 (1944), pp. 419–422.

[40] Analog Devices, *AD22100 datasheet.* http://www.analog.com/static/imported-files/data_sheets/AD22100.pdf, 2004.

[41] Texas Instruments, *Noise Analysis in Operational Amplifier Circuits - Application Report.* http://www.ti.com/lit/an/slva043b/slva043b.pdf, 2007.

[42] R. J. Barlow, *Statistics - A Guide to the Use of Statistical Methods in the Physical Sciences*, John Wiley & Sons, New York, 2013.

[43] A. D. Poularikas, *Transforms and Applications Handbook*, CRC Press, Boca Raton, Fla, 3 ed., 2009.

[44] Y. L. Luke, *The Special Functions and Their Approximations: Volume II*, Academic Press, Amsterdam, Boston, 53 ed., 1969.

[45] S. COVA *et al.*, *Avalanche photodiodes and quenching circuits for single-photon detection*, Appl. Opt., 35 (1996), pp. 1956–1976.

Acknowledgements

Erklärung

Hiermit versichere ich, dass ich diese Arbeit einschließlich beigefügter Zeichnungen, Darstellungen und Tabellen selbstständig angefertigt und keine anderen als die angegebenen Hilfsmittel und Quellen verwendet habe. Alle Stellen, die dem Wortlaut oder dem Sinn nach anderen Werken entnommen sind, habe ich in jedem einzelnen Fall unter genauer Angabe der Quelle deutlich als Entlehnung kenntlich gemacht.

Aachen, den 16. Januar 2014

Johannes Christian Schumacher